© 2017. Published by The Company of Biologists Ltd | Development (2017) 144, 4363-4376 doi:10.1242/dev.155200

RESEARCH ARTICLE

Mechanical and signaling roles for keratin intermediate filaments in the assembly and morphogenesis of *Xenopus* mesendoderm tissue at gastrulation

Pooja R. Sonavane[1], Chong Wang[1,*], Bette Dzamba[1], Gregory F. Weber[1,‡], Ammasi Periasamy[2] and Douglas W. DeSimone[1,§]

ABSTRACT

The coordination of individual cell behaviors is a crucial step in the assembly and morphogenesis of tissues. *Xenopus* mesendoderm cells migrate collectively along a fibronectin (FN) substrate at gastrulation, but how the adhesive and mechanical forces required for these movements are generated and transmitted is unclear. Traction force microscopy (TFM) was used to establish that traction stresses are limited primarily to leading edge cells in mesendoderm explants, and that these forces are balanced by intercellular stresses in follower rows. This is further reflected in the morphology of these cells, with broad lamellipodial protrusions, mature focal adhesions and a gradient of activated Rac1 evident at the leading edge, while small protrusions, rapid turnover of immature focal adhesions and lack of a Rac1 activity gradient characterize cells in following rows. Depletion of keratin (krt8) with antisense morpholinos results in high traction stresses in follower row cells, misdirected protrusions and the formation of actin stress fibers anchored in streak-like focal adhesions. We propose that maintenance of mechanical integrity in the mesendoderm by keratin intermediate filaments is required to balance stresses within the tissue to regulate collective cell movements.

KEY WORDS: *Xenopus*, Adhesion, Cadherin, Fibronectin, Gastrulation, Keratin

INTRODUCTION

Coordinated cellular movements are a key feature of many morphogenetic processes that occur in metazoan development. The cell and tissue rearrangements responsible for these movements often play out within the confined spaces of embryos, where forces generated are sensed by other proximal cells and tissues (Heisenberg and Bellaïche, 2013). These forces can also be transduced into chemical signals within cells to regulate cell behaviors that promote morphogenesis or influence gene expression (Mammoto et al., 2013; Miller and Davidson, 2013; Wozniak and Chen, 2009).

Collective cell migration is a fundamental process important in embryogenesis, wound healing and cancer cell metastasis (Friedl and Gilmour, 2009; Mayor and Etienne-Manneville, 2016). The formation and maintenance of adhesive and mechanical linkages, and the coordinated changes in cell polarity that result from these cell-cell contacts, are defining features of collectively migrating cells (Collins and Nelson, 2015). For example, in *Drosophila* border cells, a tension gradient across E-cadherin (Shotgun – FlyBase)-containing junctions has been proposed to contribute to polarization of protrusive activity at the front of the cluster where cell-cell forces are highest (Cai et al., 2014). Forces generated during collective migration of MDCK cells result in redistribution of the Hippo pathway molecule Merlin, from cell-cell junctions to the cytoplasm, where it leads to polarized Rac1 activation (Das et al., 2015). Collectively migrating cells also respond to chemotactic cues and, in many instances, a robust response to these signals requires cell-cell contact (Dumortier et al., 2012; Malet-Engra et al., 2015; Theveneau et al., 2010; Winklbauer and Selchow, 1992). How mechanical and chemical inputs are combined and processed to direct specific migration behaviors remains an important question.

Rho family GTPases are regulators of cell polarity in migrating single cells and integral to the relay of chemical and mechanical information from the extracellular matrix (ECM) to the cell interior (Ridley, 2015). Rac1 activation promotes actin polymerization, lamellipodial protrusion and integrin engagement with the ECM (Del Pozo et al., 2002). Cells that migrate collectively typically organize into leader and follower cells, and Rac1 activity is often increased in leader cells. In the case of *Drosophila* border cell migration, Rac1 activation is necessary and sufficient for leader cell behavior (Inaki et al., 2012; Wang et al., 2010; Yamaguchi et al., 2015). The importance of leader cells in generating traction forces necessary to direct migrating cohorts forward varies among tissue types. For example, specialized protrusive tip cells that lead narrow arrays of collectively migrating cells during *Drosophila* tracheal morphogenesis, and emergent migratory MDCK cells can provide the traction forces sufficient to propel both themselves and follower cells forward (Caussinus et al., 2008; Reffay et al., 2014). By contrast, both leader and follower cells in some epithelial cell sheets and in zebrafish lateral line primordia are protrusive (Farooqui and Fenteany, 2005; Haas and Gilmour, 2006). Although traction forces are typically highest along the free edges of epithelial sheets and clusters, internal cells also generate traction forces (Tambe et al., 2011; Trepat et al., 2009). Both leader and follower cells extend monopolar protrusions in *Xenopus* mesendoderm (Weber et al., 2012; Winklbauer and Nagel, 1991); however, the spatial arrangement of traction stresses in this tissue has yet to be reported. In this study, we report the spatial distribution of traction stresses applied to the substrate by migrating mesendoderm.

Xenopus mesendoderm cells migrate across the blastocoel roof (BCR) during gastrulation as a collective mass, and this basic

[1]Department of Cell Biology, School of Medicine, University of Virginia Health System, P.O. Box 800732, Charlottesville, VA 22908, USA. [2]Keck Center for Cellular Imaging, Department of Biology, University of Virginia, Charlottesville, VA 22903, USA.
*Present address: Physics Department, Central College, Pella, IA 50219, USA.
‡Present address: Department of Biological Sciences, Rutgers University-Newark, Newark, NJ 07102, USA.

§Author for correspondence (desimone@virginia.edu; dwd3m@virginia.edu)

D.W.D., 0000-0003-1926-1588

Received 23 May 2017; Accepted 25 September 2017

Development (2017) 144, 4363-4376 doi:10.1242/dev.155200

organization is maintained when mesendoderm is removed from the embryo and cultured intact on a fibronectin (FN) substrate. C-cadherin (Cdh3 – Xenbase) adhesions are required to maintain cell cohesiveness and the extension of monopolar protrusions, which contact and adhere to FN (Winklbauer and Nagel, 1991) using α5β1 integrins (Davidson et al., 2002). These cells become multipolar protrusive on FN when cell-cell adhesive contacts are disrupted following tissue dissociation in low Ca^{2+} (Winklbauer and Selchow, 1992). Local 'tugging' forces on C-cadherin adhesions at the rear of a single mesendoderm cell are sufficient to recruit keratin 8 intermediate filaments (IFs) and plakoglobin (γ-catenin) to sites of stressed adhesions and restore monopolar protrusive activity (Weber et al., 2012). Expression of keratin 14 in leader cells has also been reported to be essential for the collective dissemination of tumor cell clusters in a mouse model of breast cancer (Cheung et al., 2013, 2016). These data suggest that keratin IFs may be integral players in a range of collective cell migration events.

In serum-starved nonmotile cells, vimentin IFs extend throughout the cell (Helfand et al., 2011; Valgeirsdóttir et al., 1998). Upon serum addition or activation of the small GTPase Rac1, vimentin IFs disassemble and protrusive lamellipodia form. Specific disruption of the vimentin IF network also promotes the formation of lamellipodia around the cell suggesting that Rac1 and vimentin are functionally antagonistic (Helfand et al., 2011). Whether keratin IFs display a similar antagonism with Rac1 is unknown.

In this study, we report that keratin IFs maintain mechanical linkages between cells that are required for normal collective cell migration behaviors including the regulation of cell-cell and cell-ECM adhesion, cytoskeletal organization and cell contractility. The integrity of these mechanical connections is crucial for the higher-order assembly and morphogenesis of mesendoderm tissue at gastrulation, as well as the spatial regulation of Rac1 GTPase activity.

RESULTS

A role for keratin IFs in the spatial regulation of traction forces in migrating mesendoderm

The protrusive and motile behaviors of individual cells in intact *Xenopus* mesendoderm suggest that traction stresses are distributed throughout the tissue and required for collective movement (Davidson et al., 2002). Based on these observations and analyses of collectively migrating MDCK cells (Trepat et al., 2009), we hypothesized that traction stresses are likely to be greatest at the leading edge of the mesendoderm and progressively decrease in subsequent rows of cells, where cumulative traction stresses would be balanced by increasing cell-cell stresses (Weber et al., 2012). In order to test this model directly, we adapted traction force microscopy (TFM) methods to map the distribution of traction stresses generated by individual cells within explants migrating on deformable FN substrates. In this approach, a polyacrylamide substrate of known elastic modulus is prepared with embedded fluorescent beads, which serve as fiducial marks. The TFM substrate is coated with fibronectin and mesendoderm explants allowed to attach. Explant cells deform the substrate as they migrate and the resulting displacements of the embedded beads are recorded using a confocal microscope. Traction forces are derived from these data utilizing Fourier transform traction cytometry (Butler et al., 2002). Additional details are provided in the Materials and Methods. The explant preparations used in this study [i.e. dorsal marginal zone (DMZ) and 'donut' explants] are described in Davidson et al. (2002) and summarized in Fig. S1.

Average radial traction stresses (vector values) within DMZ explants are concentrated along the leading row (green highlighted area between Fig. 1A-C and Fig. 1G), and are reduced significantly in the second row (yellow highlighted area between Fig. 1A-C) and beyond. 'Stress maps' were further binned into 10 µm strips starting with, and outlined by, the leading edge of the explant (Fig. 1A; white dotted lines are separated by 50 µm, the approximate width of one row of cells). Averages of vector (Fig. 1B,G) and absolute (Fig. 1C,H) values of traction stresses were calculated for each 10-µm binned region. The leading protrusive edge of the tissue generates the highest traction stresses (absolute traction stresses; Fig. 1C) contributing to directional migration (positive vector values indicate net traction stresses that contribute to forward migration, i.e. ∼180 Pa; Fig. 1B). Following rows exert lower traction

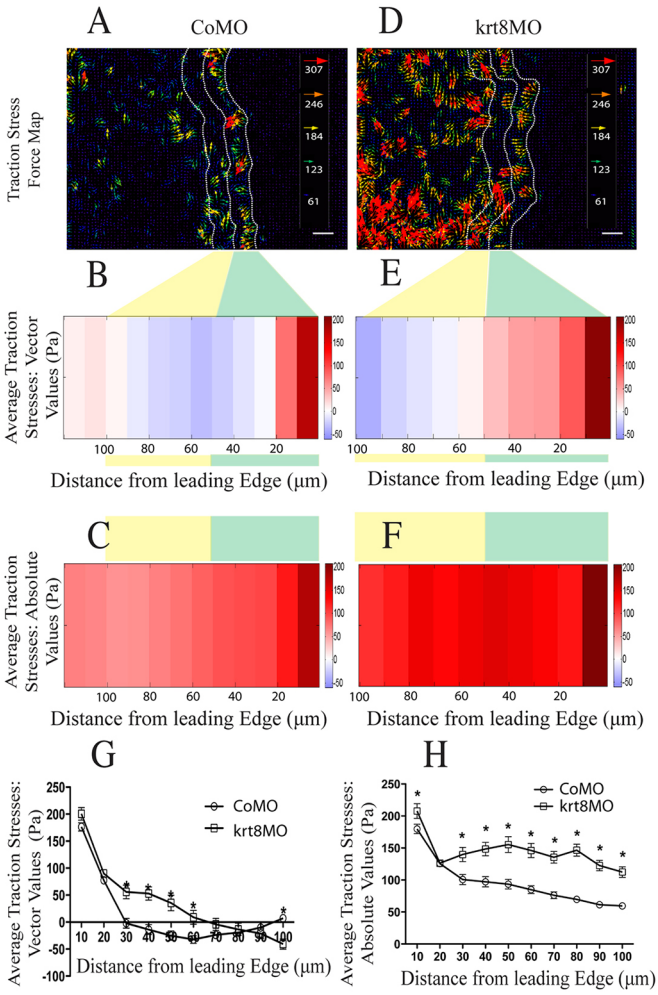

Fig. 1. Distribution of traction stresses in control and keratin morphant explants on FN substrates. (A,D) Representative traction stress maps for control (A) and krt8 morphant (D) mesendoderm explants. Arrows indicate the magnitudes and directions of traction stresses. The distance between white dotted lines, 50 µm, is approximately the width of one cell row. Green and yellow highlighted areas between vertical panels correspond to leading and second rows of cells, respectively. Heat maps were binned into 10-µm slices starting from the leading edge. (B,C,E,F) Average vector (B,E) and absolute (C,F) values of traction stresses for each 10 µm slice, plotted as kymographs. Kymographs of average vector values of traction stresses correspond to the heat maps of control (B) and krt8 morphants (E). Kymographs of average absolute values of traction stresses corresponding to the heat map of control (C) and krt8 morphants (F). (G,H) Comparisons of average vector (G) and absolute (H) values of traction stresses for two time-points from three separate control and krt8 morphant explants (data are mean±s.e.m., **P*<0.05). Scale bars: 50 µm.

Development (2017) 144, 4363-4376 doi:10.1242/dev.155200

stresses (average absolute traction stresses; Fig. 1C,H), and the vectors of these traction stresses are randomized and cancel as reflected in the preponderance of zero to negative values for the binned vector traction stresses (Fig. 1B,G). These data suggest that cells in following rows migrate randomly or are being 'dragged' along by leading edge cells. This confirms that directional traction stresses responsible for forward migration originate at the leading edge and are not distributed throughout the tissue.

The geometry of the mesendoderm and its substrate, the BCR, differs markedly from a DMZ explant on a plastic or glass surface. In the embryo, mesendoderm consists of a circumferential ring of tissue, separated from the BCR by the cleft of Brachet as it begins to migrate along the dorsal side of the embryo, spreading laterally to the ventral margin of the tissue as gastrulation progresses. This 'donut' of tissue can be removed and placed on a FN substrate for further analysis (Fig. S1B). We next addressed whether the traction stresses generated by mesendoderm in the donut configuration are comparable to those of the DMZ (Fig. S2). Like the DMZ, highest traction stresses are generated by leading row cells; however, the distribution of these stresses is not symmetrical. Traction stresses are greatest on the anterior-dorsal side and weakest on the posterior-ventral side (Fig. S2A). In addition, the magnitudes of these stresses vary depending on the extent of closure. Average radial traction stresses are ∼30% of those observed in DMZ explants as migration begins, and increase as closure proceeds, ultimately matching those of DMZ explants just prior to closure, when traction stresses again decrease (Fig. S2B). These data suggest that donut explants do not require large radial traction forces to close.

Reduced expression of newly synthesized keratin IFs results in misdirected cell protrusions in intact mesendoderm and failure of individual cells to repolarize in response to local tugging forces on C-cadherins (Weber et al., 2012). To investigate whether these changes in protrusive behaviors are reflected in the magnitude and/or direction of traction stresses, we used a previously reported antisense morpholino directed against the 5′-UTR of keratin 8 (krt8) to knock down expression. Keratin IFs are obligate heteropolymers of type I acid and type II basic subunits, and krt8 is the only type II basic keratin expressed at gastrulation (Franz and Franke, 1986; Franz et al., 1983). Thus, knockdown of krt8 effectively inhibits the assembly of new keratin IFs. High traction stresses are not limited to the leading row in krt8 morphants (green highlighted area between Fig. 1D-F). Although reduced relative to the first row, traction stresses in the second row of these explants (e.g. yellow highlighted area between Fig. 1D-F), remain significantly higher than follower rows in control morphants (Fig. 1C,F,H). However, average vector traction stresses reveal many randomly directed forces (high negative and positive values of vector sums; Fig. 1E,G), which in some cases are canceled out by balancing forces in opposing directions. This likely contributes to the observed decrease in the overall rate of tissue migration in krt8 morphants (Fig. S3). Average traction stresses from two time points of three separate explants are expressed as vector (Fig. 1B,E,G) and absolute (Fig. 1C,F,H) values. Based on these results, we conclude that keratin IFs are important for maintaining the normal spatial distribution of cellular traction stresses across a collectively migrating mesendoderm explant.

Leading edge and following row cells display differences in protrusive behavior and Rac1 activity

We next addressed whether the protrusion morphology of cells in the leading edge and following rows correlates with the distribution of traction stresses obtained by TFM. Transcripts encoding GFP-tagged α5 integrin (α5-GFP), along with LifeAct-mCherry (Riedl et al., 2008), were injected into early cleavage stage blastomeres. At stage 11, DMZ explants were prepared and plated on FN; both cell-substrate adhesions and actin were then visualized using total internal reflection fluorescence (TIRF) microscopy. Leading edge cells in controls extend broad lamellipodia containing an actin meshwork and α5-GFP in focal adhesions (Fig. 2A-C). Occasional filopodia are also seen in the leading edge cells of the mesendoderm during migration (Movie 1). However, following row cells have smaller lamellipodia and extend long filopodial protrusions (Movie 2) enriched with both integrin α5-GFP and actin (Fig. 2D-F). Following row cells extend more filopodial processes per cell and the average length of these processes is significantly greater than the filopodia of leading edge cells (leading edge, 6.96±0.3 µm; following row, 11.06±0.5 µm), with some extending up to 30 µm in length (Fig. 2G). Scanning electron microscopy of fixed and fractured embryos confirms the presence of comparable length filopodia *in vivo* (Fig. 2H) in following row cells (e.g. compare Fig. 2I and J). These structures extend and make contact with neighboring cells (Fig. 2J). Time-lapse TIRF imaging of mesendoderm cells expressing membrane-EGFP revealed that these filopodia are highly dynamic, and in following row cells they were observed to curve and spiral frequently as they grow in length (Movie 2). Overall, lamellipodial protrusions in following row cells are less persistent than in leading edge cells and undergo frequent direction changes (Fig. 2K). In addition, physical removal of leading edge cells caused following row cells to lose filopodia, repolarize and adopt the behavior of a new leading edge with lamellipodia and few filopodia (Fig. S4).

Because Rac1 is a known regulator of actin polymerization and lamellipodia (Ridley et al., 1992), we next addressed whether observed differences in protrusive behaviors between leading edge and following row cells correlate with differences in Rac1 activity. To resolve spatial differences in Rac1 activity, FRET microscopy was performed on mesendoderm cells expressing a Rac1 biosensor (Hodgson et al., 2001). In leading edge cells of the mesendoderm, Rac1 is widely distributed throughout the cell (Fig. 2L). However, a gradient of Rac1 activity is observed in these cells with highest FRET efficiency noted in lamellipodia at the leading edge (Fig. 2M,P). The Rac1 biosensor is also distributed throughout following row cells but we failed to observe a polarized gradient of Rac1 activity in these cells (Fig. 2N,O,P).

Spatial regulation of focal adhesion dynamics is altered in keratin IF-depleted mesendoderm

These results reveal significant differences between leader and follower row cells with respect to the distribution of traction stresses generated, and the protrusions observed. We next explored whether differences in focal adhesion (FA) dynamics between normal leader and follower cells, and cells with reduced keratin IF expression, could help explain these behaviors. Mesendoderm explants expressing EGFP-paxillin, a marker of FAs (Turner, 2000), and LifeAct-mCherry, were imaged using TIRF. Mature persistent FAs were evident in forward protrusions with few FAs noted in the cell body away from the leading edge (Fig. 3A,K; Movie 3). Actin in these cells forms a branched network that colocalizes with paxillin at sites of FAs (Fig. 3B,B′,B″). Both FA area (Fig. 3I, leading edge CoMO=0.3874±0.02 µm^2) and numbers (Fig. 3J, leading edge CoMO=111.9±8.9 FAs per cell) are greatest in forward protrusions of leading edge cells, coincident with highest traction forces (Fig. 1A-C). By contrast, following row cells have fewer FAs (Fig. 3J, following row CoMO=43.42±4.3 FAs per cell), are reduced in area (Fig. 3I, following row CoMO=0.2374±0.01 µm^2)

Development (2017) 144, 4363-4376 doi:10.1242/dev.155200

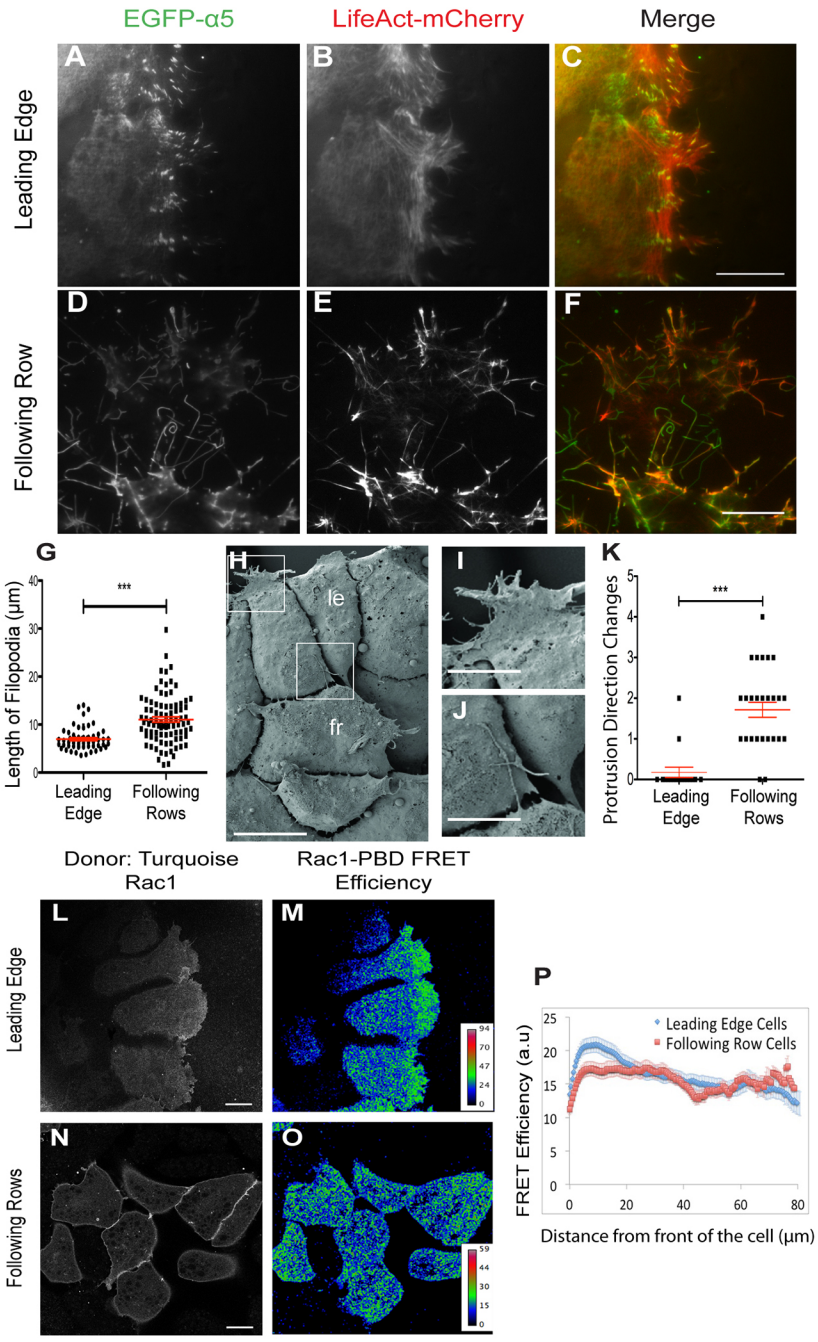

Fig. 2. Mesendoderm cells organize into leader and follower cells with distinct protrusive morphologies. (A-F) Representative TIRF images of leading edge (A-C) and following row (D-F) cells: α5 integrin-EGFP (A,D); mCherry-LifeAct (B,E); merged images (C,F). (G) Quantification of filopodial lengths in leading edge and following row cells. Number of filopodia analyzed: leading edge=57; following row=88 (data are mean±s.e.m., ***P<0.001, expressed as dot plots). (H) Scanning electron micrograph of *Xenopus* mesendoderm, BCR-facing side. fr, following row; le, leading edge. (I,J) Magnified views of the boxes in H, showing lamellipodia of leading edge cells (I) and specialized filopodia in following row cells (J). (K) The number of times a cell protrusion changes direction over the course of 5 min. TIRF images of cells expressing membrane-EGFP were used to track individual protrusions (six to nine individual explants were imaged across two to three separate experiments; data are mean±s.e.m., ***P<0.001). (L-O) FRET microscopy of Rac1 activity in leading edge (L,M) and following row (N,O) cells on FN. Confocal images were taken 1 h after plating explants on FN: Turquoise-Rac1 (L,N); Rac1-PBD FRET efficiency (M,O) (15 individual explants were imaged across five separate experiments). (P) Graph showing the distribution of FRET efficiency within individual cells. Data are mean±s.e.m. (15 individual explants were imaged across five separate experiments; total numbers of individual cells analysed: leading edge=77; following row=37). Scale bars: 25 μm in C, F, H, L and N; 10 μm in I and J.

and more dispersed throughout the cell body (Fig. 3C). Similar to leading edge cells, branched actin in following row cells colocalizes with paxillin at FAs (Fig. 3D,D′,D″). FAs in following row cells are highly dynamic with smaller, nascent contacts assembling and disassembling rapidly, suggesting lower overall adhesion to the substrate (Movie 4). This is consistent with reduced traction stresses noted in following row cells (Fig. 1A-C,G).

Krt8 morphant cells have misdirected protrusions (Weber et al., 2012), with both leader and follower cells exerting high traction stresses (Fig. 1D-F,G). These changes in behavior relative to controls are also reflected in both the formation and dynamics of FAs. TIRF images and time-lapse movies (Movies 5 and 6) reveal that leading edge cells in krt8 morphants form fewer FAs relative to controls (Fig. 3J, 77.63±8.1 versus 111.9±8.9) but FA area is significantly increased (Fig. 3I, 0.517±0.04 μm^2 versus 0.3874±0.02 μm^2). These large mature FAs are present in both forward-facing and misdirected protrusions, and at the cell rear in both leading (Fig. 3E,F,F″,K; Movie 5) and following (Fig. 3G,H,H″; Movie 6) rows. Prominent actin stress fibers anchored in FAs extend across the long axes of these cells (Fig. 3E-F′,G-H′, see also Fig. 4). FA area and number are minimally changed between leading edge and following row cells of krt8 morphants (Fig. 3I,J), unlike in controls. These data indicate the importance of keratin IFs in maintaining the ‘row-specific’ differences in cell behaviors and overall organization of mesendoderm.

Prominent actin stress fibers are observed upon depletion of keratin IFs

Because TIRF limits visualization to within 100 nm of the FN-coated glass surface, we used confocal microcopy to investigate the

Development (2017) 144, 4363-4376 doi:10.1242/dev.155200

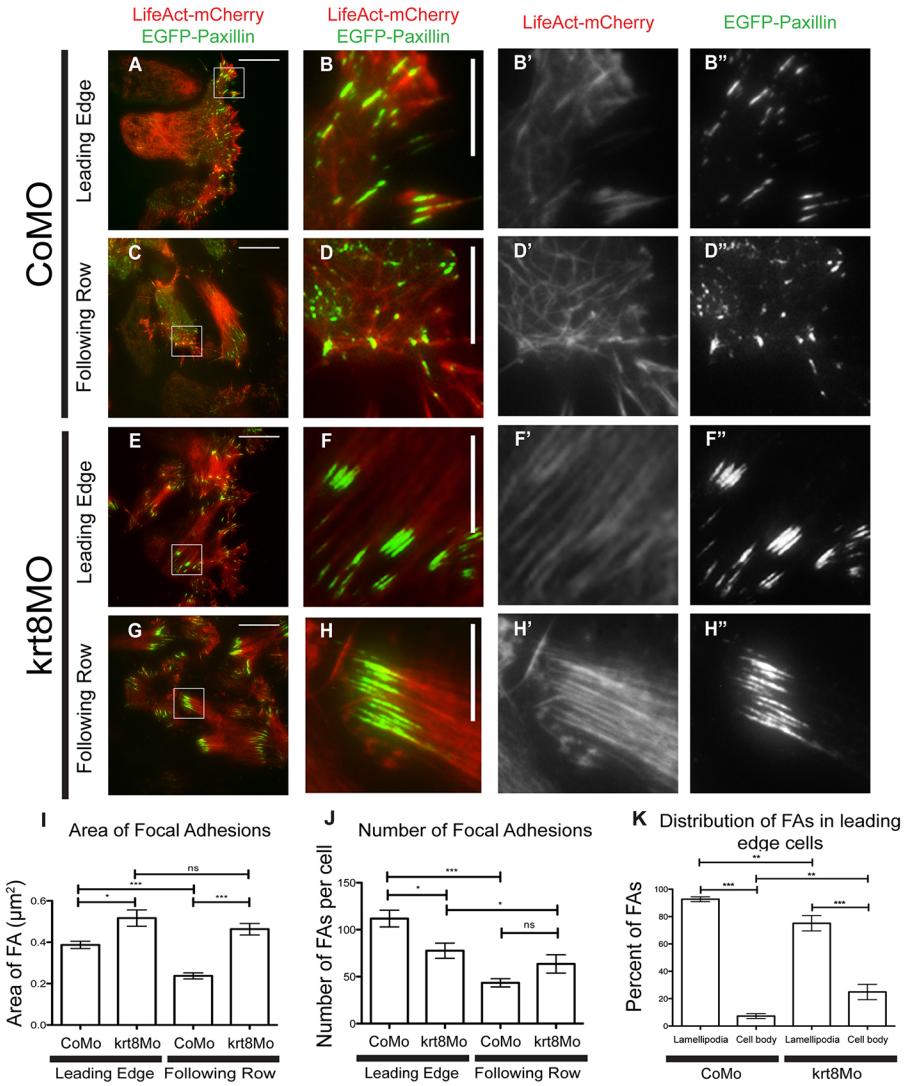

Fig. 3. Focal adhesion dynamics and actin cytoskeleton are altered in krt8 morphant explants. (A,C,E,G) Representative TIRF images of mesendoderm explants expressing LifeAct-mCherry (red) and EGFP-paxillin (green). (B-B″,D-D″,F-F″,H-H″) Magnified views of the boxes in A, C, E and G, corresponding to merged (B,D,F,H) and separate LifeAct-mCherry (B′,D′,F′,H′) and EGFP-paxillin (B″,D″,F″,H″) channels. (I-K) Quantifications of FA area (I), FAs per cell (J) and distribution of FAs within cells (K), calculated from the first frames of nine movies for each condition (Movies 3-6) (nine individual explants per condition were imaged across three separate experiments; data are mean±s.e.m. **P*<0.05; ***P*<0.01; ****P*<0.001; ns, not significant). Scale bars: 25 µm in A, C, E and G; 10 µm in B, D, F and H.

deeper organization of actin filaments in both fixed and live mesendoderm explants. As reported previously (Bjerke et al., 2014), a dense meshwork of actin is present within the large monopolar, lamellipodia that form along the leading edge of control explants in the direction of travel (Fig. 4A,B). These actin-filled processes protrude persistently in the forward direction with fine cortical actin filaments evident throughout the cell body (Movie 7). Protrusions in following row cells (Fig. 4A,C, arrows) are smaller, highly dynamic and less persistent than those in the leading row; long filopodia noted in Fig. 2D-F are also evident in these cells (Fig. 4A,C, arrowheads).

Knockdown of keratin IFs (Fig. 4E-H, krt8MO) results in dramatic changes in cell shape and actin organization. Parallel stress fibers extending throughout the cell body are noted in both leading and following row cells (Fig. 4E-G). Protrusions are often misdirected in these cells, particularly in the leading row (Fig. 4E, F) (see also Weber et al., 2012). Cell protrusions are typically smaller than those observed in control explants, but they are highly dynamic and appear to apply tugging forces on neighboring cells (Movie 8). Acrylamide (nonpolymerized) can also be used to disrupt intermediate filaments acutely in cells (Eckert and Yeagle, 1988). Mesendoderm explants exposed to increasing concentrations of acrylamide underwent a rapid reorganization of the actin cytoskeleton, from dense actin meshwork in protrusions and fine cortical filaments in the cell body to long stress fibers (Fig. S5). Overall, the appearance of acrylamide-treated cells closely matches that of keratin morphant explants and supports the specificity of the krt8 morphant phenotype.

Maintenance of cell cohesion is essential for collective migration and in *Xenopus* mesendoderm, this involves maintenance of C-cadherin-based adhesion complexes linked to both actin and keratin IFs (Weber et al., 2012). Fine cortical actin filaments are apparent at cell-cell junctions in controls; however, in krt8 morphant cells the morphology of these junctions is altered (Fig. 4D,H); actin stress fibers now span the cells and appear continuous with their neighbors (Fig. 4H).

Phosphomyosin light chain II levels are upregulated in krt8 morphant explants

The appearance of streak-like focal adhesions (Fig. 3E-H″) and actin stress fibers (Fig. 4E-H) in krt8 morphants suggests that contractility is increased in these cells (Even-Ram et al., 2007). Actin association with myosin and phosphorylation of myosin light chain II are essential for regulating cell contractility during migration (Vicente-Manzanares et al., 2009) and in response to changes in ECM stiffness (Clark et al., 2007). To address whether actomyosin contractility was increased in krt8 morphants, phosphomyosin light chain II (pMLC) levels were quantified by

Development (2017) 144, 4363-4376 doi:10.1242/dev.155200

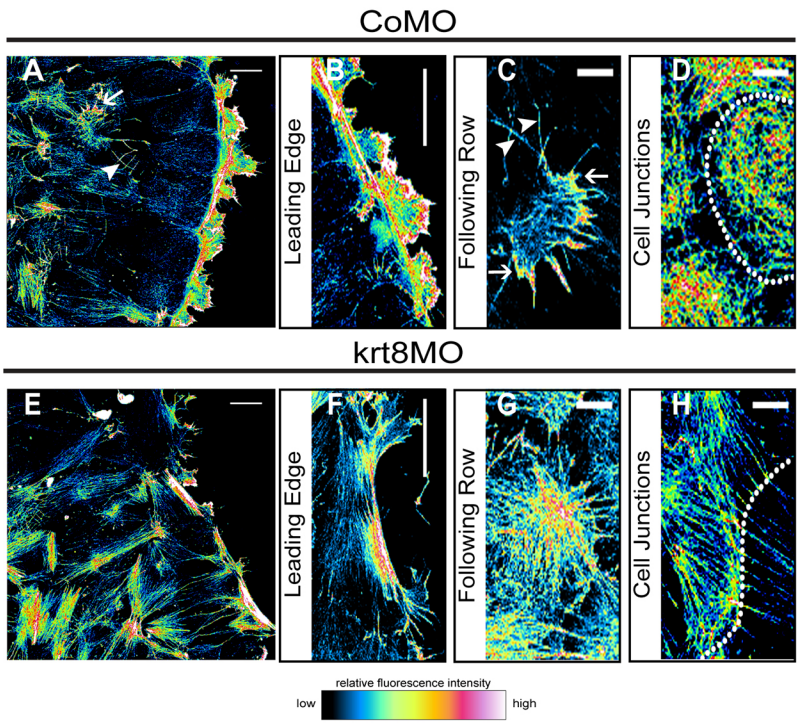

Fig. 4. Actin stress fibers predominate in mesendoderm explants from keratin morphant embryos. (A-H) Confocal projections of phalloidin-stained control (A-D) and krt8 morphant (E-H) explants on FN. Pseudocolors correspond to fluorescence intensity heat map. Collapsed *Z*-stack images of representative explants at low magnification (A,E), leading row lamellipodia (B,F), following row protrusions (C,G) and cell-cell junctions (D,H). Arrowheads in A and C indicate specialized filopodia; arrows indicate small protrusions. Dotted lines in D and H indicate borders between two cells (six individual explants per condition were imaged across two separate experiments). Scale bars: 25 µm in A, B, E and F; 10 µm in C, D, G and H.

western blotting (Fig. 5A-D). Because mesendoderm explants also contain nonmigrating ectodermal tissue, mesendoderm from control and krt8 morpholino-injected embryos was specifically dissected, dissociated and plated at subconfluent densities on stretchable silicone membranes coated with either FN (to mimic cell-ECM interaction) or C-cadherin (C-cad-FC, to mimic cell-cell interaction). Cells attach and spread on both FN and C-cad-FC substrates but appear more symmetrical on C-cad-FC than on FN (Fig. S6). After 1 h, half the cultures were subject to cyclical rounds of uniaxial stretch and the remainder were left 'unstretched'. Stretching was performed to simulate the tension experienced by adhesions (cell-matrix or cell-cell) during migration.

pMLC levels increased two- to threefold in control cells stretched on FN (Fig. 5A,B). No increase in pMLC was detected when cells were instead stretched on C-cad-FC (Fig. 5C,D). By contrast, pMLC was increased in krt8 morphant cells adherent to either FN or C-cad-FC substrates in the absence of stretch. Unlike the situation for CoMO cells on FN, stretching krt8 morphant cells did not further increase pMLC levels. The 'stretch-independent' enhancement of pMLC in krt8 morphant cells required specific adhesion to either C-cadherin or FN substrates; no significant increase in pMLC was observed when krt8 morphant cells were kept in suspension (Fig. 5A-D). Thus, mesendoderm cells respond specifically to mechanical deformations of the FN substrate by becoming more contractile. Notably, however, knockdown of keratin IFs can result in a similar increase in pMLC levels and contractility in the absence of applied stretch, consistent with observed changes in traction stresses, actin filament organization and focal adhesion dynamics (Figs 1, 3 and 4).

Inhibition of myosin light chain II activity inhibits formation of actin stress fibers in krt8 morphants

Keratin-depleted cells are more contractile, exert higher traction stresses and form larger, more mature focal adhesions than controls. pMLC is known to be essential for FA maturation and inhibition of myosin II activity reduces FA area (Pasapera et al., 2010). We next asked, therefore, whether inhibiting myosin II activity would reverse some of the features of keratin knockdown including stress fiber formation. Mesendoderm explants were treated with the ROCK inhibitor Y27632 to inhibit MLC phosphorylation and then fixed and stained with phalloidin. Leading edge cells from control (CoMO) explants revealed the typical arrangement of actin meshwork in lamellipodia and fine cortical actin filaments throughout cell bodies (Fig. 5E). The addition of Y-27632 had no appreciable effect on overall morphology or actin organization in these cells (Fig. 5F), which maintained actin-rich, broad lamellipodial protrusions along the leading edge and smaller protrusions in following row cells. By contrast, the cell bodies of krt8 morphant cells contained abundant actin stress fibers in both leading and following row cells (Fig. 5G,I). Treatment of krt8 morphant explants with ROCK inhibitor suppressed stress fiber formation, increased cortical actin filaments, and leading edge cells regained actin-dense lamellipodia (Fig. 5H,I). These data indicate that inhibition of myosin II activity is sufficient to block actin stress fiber formation and the increased cell contractility that accompanies keratin IF knockdown.

Functional antagonism of keratin IFs and Rac1

As described previously, a 'basket-like' arrangement of keratin IFs forms at the rear of mesendoderm cells undergoing collective cell migration (Weber et al., 2012), and this arrangement is most pronounced in the leading row cells, which are also notable for the broad monopolar-directed lamellipodial protrusions they extend in the direction of travel. Rac1 GTPase activity is highest in these forward protrusions and decreases toward the cell rear (Fig. 2L,M,P). Helfand et al. (2011) have reported that Rac1 and vimentin IFs are functionally antagonistic. Given the spatial arrangement of keratin IFs and Rac1 GTPase activity in the mesendoderm, we asked whether similar opposing functions might be operating in these cells. The Rac1 FRET biosensor was expressed in control and krt8 morphants and Rac1 GTPase activity imaged (Fig. 6A-D). As described in Fig. 2, Rac1 activity in controls is highest in

Development (2017) 144, 4363-4376 doi:10.1242/dev.155200

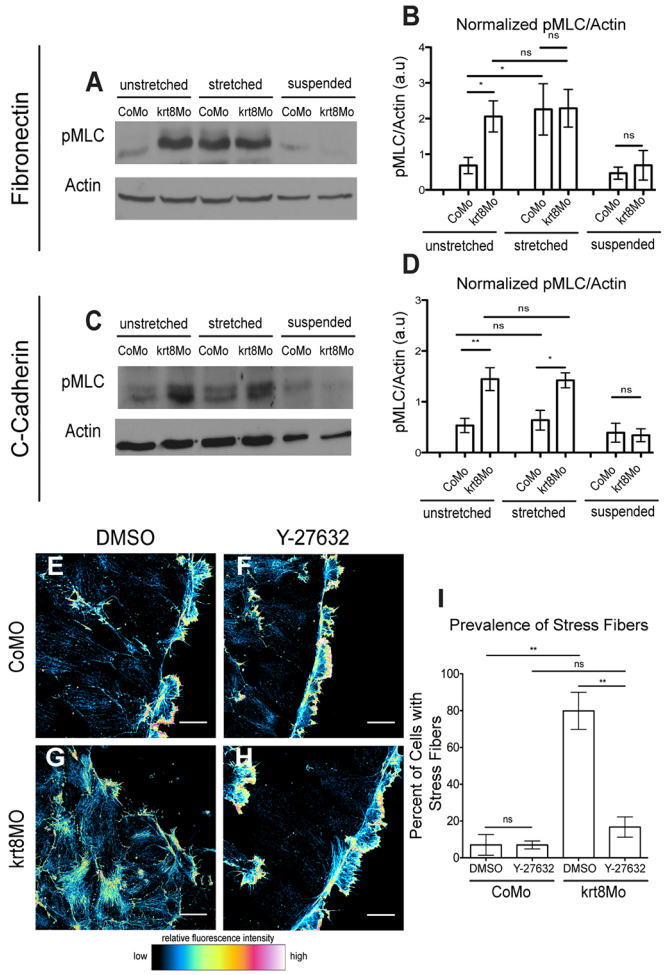

Fig. 5. pMLC is upregulated in keratin morphant mesendoderm. (A,C) Representative western blots of pMLC levels in control and krt8 morphant-dissociated mesendoderm cells. Silicone stretchers were coated with FN (A) or C-cad-FC (C). Following 1 h attachment, cells were subjected to 15 rounds of 10% cyclical stretch. Cell lysates were made immediately after stretching. Blots were then probed with antibodies against pMLC (S19) and actin. (B,D) Quantification of pMLC levels normalized to actin (n=5 for FN and n=4 for C-cad; data are mean±s.e.m. *P<0.05; **P<0.01; ns, not significant). (E-H) Confocal projections of phalloidin-stained explants on FN after 1 h treatment with Y27632 (10 µM) or DMSO. Pseudocolors correspond to the fluorescence intensity heat map. Control explant treated with DMSO (E) or 10 µM Y27632 (F); krt8 morphant explant treated with DMSO (G) or 10 µM Y27632 (H) (nine individual explants per condition were imaged across three separate experiments). (I) Percentage of cells with stress fibers in control and krt8 morphant explants treated with 10µM Y27632 or DMSO (number of cells counted: CoMO_DMSO=68, CoMO_Y27632=81, krt8MO_DMSO=59, krt8MO_Y27632=91; data are mean±s.e.m. **P<0.01; ns, not significant). Scale bars: 25 µm.

lamellipodial protrusions at the cell front and lowest at the cell rear (Fig. 6A,B,E). In krt8 morphant explants, the gradient of Rac1 GTPase activity evident in controls is lost (Fig. 6C,D,E). Thus, absence of a Rac1 activity gradient in these cells is correlated with krt8 knockdown and consistent with the possible functional suppression of Rac1 activity by the keratin cytoskeleton.

We performed the converse experiment by expressing a photoactivatable, constitutively active form of Rac1 (mCherry-PA-Rac1Q61L; Wu et al., 2009) along with EGFP-krt8 to visualize keratin filaments. A region of interest (ROI) was selected for irradiation at 456 nm with a confocal microscope. Activation of mCherry-PA-Rac1 leads to the local formation of a membrane ruffle and lamellipodia within 3 min of irradiation (Fig. 6F-H, arrowheads). In addition, activation of PA-Rac1 is accompanied by the loss of EGFP-keratin IFs within the ROI in proximity to the newly formed protrusions (Fig. 6G,H,L; Movie 9). A nonphotoactivatable Rac1 construct (mCherry-PA-Rac1C450A) was co-expressed along with EGFP-krt8 as a control and irradiated as described. No protrusions were induced within the ROI of control cells following irradiation (Fig. 6I-K). Moreover, EGFP-keratin filaments were maintained in the irradiated ROI (Fig. 6I-L), confirming that loss of EGFP-keratin filaments in Fig. 6F-H was not the result of photobleaching or photo damage (Movie 10). These data support the conclusion that keratin IFs and active Rac1 have opposing roles in the mesendoderm.

DISCUSSION

Traction stresses are generated primarily by leading edge cells in the mesendoderm

A primary goal of this study was to establish the importance of cell-ECM traction forces in the assembly, organization and collective progression of mesendoderm cells across the BCR at gastrulation. It is well established from mammalian cell culture studies that both the leading and trailing edges of migrating single cells exert traction on the ECM (Lauffenburger and Horwitz, 1996; du Roure et al., 2005). In collective modes of cell migration, the generation of traction forces by cells at the free or leading edge, are typically balanced by cell-cell adhesions at the rear (Weber et al., 2012) and in some instances, at lateral contacts between cells. The extent to which directed cohesive migration involves the active ‘tugging’ of one cell upon another versus the coordinated ‘crawling’ of independent cells (Farooqui and Fenteany, 2005; Tambe et al., 2011; Trepat et al., 2009) is not always clear, and likely varies with cell and tissue type and the presence or absence of directional cues arising from chemokine signaling (Nogare et al., 2014). Based on earlier observations (Davidson et al., 2002), we proposed a distributed traction model to explain mesendoderm collective migration (Weber et al., 2012). This model predicts that highest traction stresses are generated by cells at the leading edge with following rows of cells displaying progressively lower tractions. Correspondingly, cell-cell stresses are progressively increased in succeeding rows, reflecting the balancing of accumulated traction stresses at any given position away from the leading edge (Trepat et al., 2009). Other collectively migrating cells and tissues are known to rely on leader cells that pull follower cells forward (Brugues et al., 2014; Rausch et al., 2013; Tse et al., 2012).

TFM experiments (Fig. 1; Fig. S2) revealed that traction stresses are being generated along the leading edge of the first row of cells but are largely absent in the second row and beyond, in contrast to what is predicted by a distributed traction mechanism. This indicates that leading row traction forces are being balanced by cell-cell adhesive contacts with the follower rows. Thus, leader cells are actively pulling the following row cells along, and follower row substrate tractions are not a major contributor to the forward migration of the mesendoderm. It is not yet possible to measure traction forces in the embryo, but there are two pieces of evidence depicted in Fig. 7 that support the conclusions arising from the explant studies. First, bisection of live embryos at gastrula stages reveals the presence of a clear, expanded ‘space’ (i.e. the cleft of Brachet) between the mesendoderm tissue and the BCR in agreement with the lack of detectable traction stresses in following row cells of explants on FN (Fig. 1). However, the leading-edge of the mesendoderm, which defines the forward boundary of the cleft, is tightly adherent to the BCR and resists physical separation (P.R.S. and B.D., unpublished). Second, Moosmann et al. (2013)

Development (2017) 144, 4363-4376 doi:10.1242/dev.155200

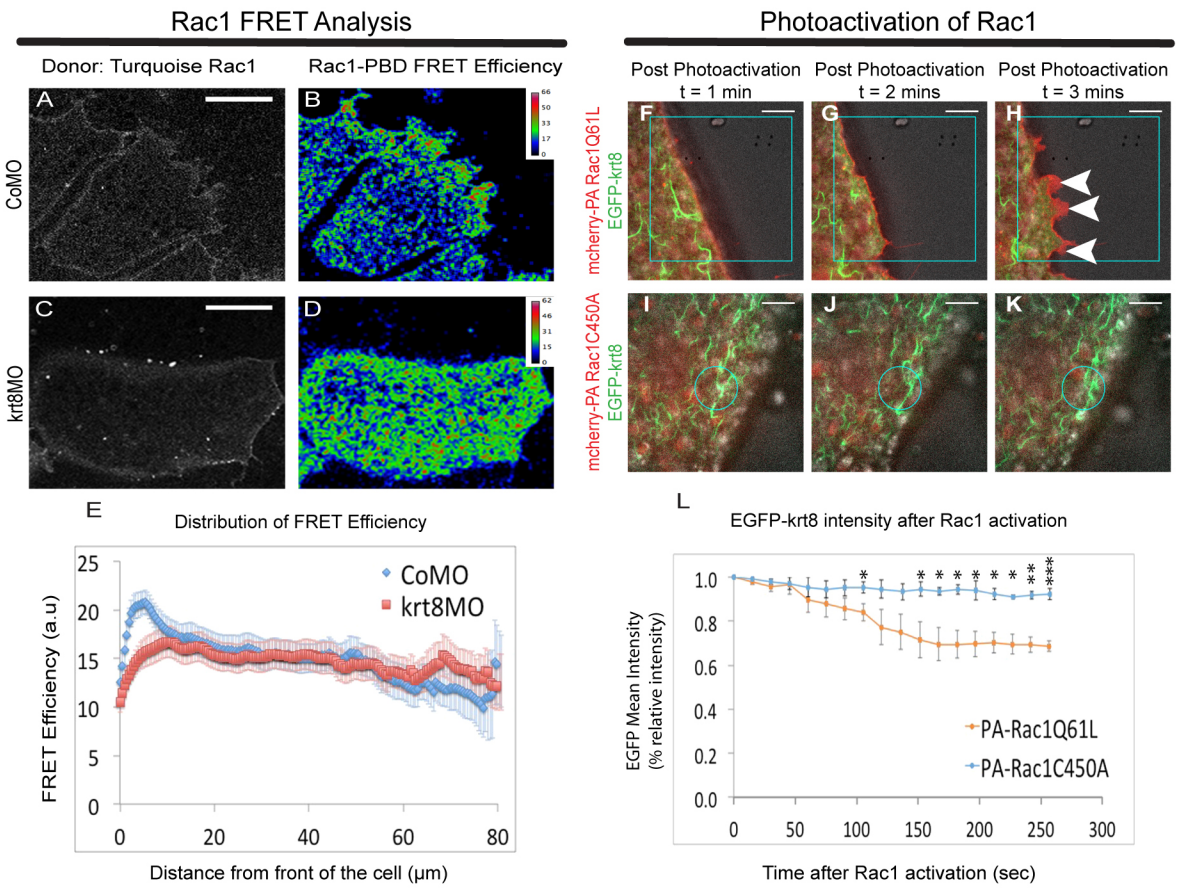

Fig. 6. Mutual antagonism of Rac1 GTPase activity and keratin IFs in leading edge mesendoderm. (A-D) FRET analysis of Rac1 activation in control and krt8 morphant mesendoderm. Confocal FRET imaging 1 h after plating DMZ explants on FN. Control (A,B) and krt8 morphant (C,D) explants showing distribution of donor Turquoise-Rac1 (A,C) and Rac1-PBD FRET efficiency (B,D) (nine individual explants per condition were imaged across four separate experiments). (E) Graph showing the distribution of FRET efficiency within leading edge cells in control and krt8 morphant explants. Data are mean±s.e.m. (total number of cells analysed: CoMo=24; krt8MO=29). (F-K) Confocal images of photoactivation of Rac1 in dissociated mesendoderm cells expressing mCherry-PA-Rac1Q61L (red) and EGFP-krt8 (green) (F-H) or nonphotoactivatable mCherry-PA-Rac1C450A (red) and EGFP-krt8 (green) (I-K). Regions irradiated with a 456 nm wavelength laser are indicated (boxes in F-H and circles in I-K). Times following irradiation: t=1 min (F,I); t=2 min (G,J); t=3 min (H,K). (L) Intensity of EGFP-krt8 after activation of photoinducible Rac1 constructs (three cells were analyzed per condition; data are mean±s.e.m. *P<0.05; **P<0.01; ***P<0.001). Scale bars: 25 μm.

used x-ray microtomography to image internal tissue movements of intact living gastrula-stage embryos; these data confirm the separation of follower rows of mesendoderm cells from the BCR, and also the tight association of the leader row cells. Moreover, inward deformation of the BCR at the site of contact with the leading row suggests not only strong adhesion but also that the mesendoderm is under considerable anisotropic tension oriented in the direction of travel, in agreement with explant studies (Davidson et al., 2002). Taken together, these data suggest that high traction stresses in the leading edge are borne by cell-cell stresses in the follower rows and, moreover, that this distribution of forces is required for overall organization of the tissue.

The high traction stresses resolved at the leading edge correlate with the presence of large, mature FAs. Cells exert traction stresses on the ECM through their integrin-based FAs (Lauffenburger and Horwitz, 1996), and transmission of forces to the ECM via these adhesions is essential for FA maturation (Chrzanowska-Wodnicka and Burridge, 1996; Pasapera et al., 2010; Plotnikov et al., 2012; Roca-Cusachs et al., 2013) and forward cell migration (Beningo et al., 2001). Follower row cells form smaller and fewer FAs, consistent with the inability of these cells to generate significant traction stresses. However, if the leading row is physically removed from a migrating DMZ explant, the following row cells quickly transform their morphology to become indistinguishable from the cells that they replaced in terms of protrusive activity and appearance of larger, mature FAs (Fig. S4). This suggests that follower row cells are normally unable to exert substrate traction forces sufficient for FA maturation, owing to the high cell-cell stresses they experience as a consequence of their position behind the leading row. Cadherin adhesion is also reported to antagonize cell-matrix adhesions (Borghi et al., 2010; Mertz et al., 2013). Together, these might explain why the following row cells do not adhere strongly to the BCR in the embryo.

Following row cells also extend long, highly dynamic filopodia (Fig. 2; Movie 2). Their function in the mesendoderm is not known, but, based on evidence from other systems, they could be involved in morphogen signaling (Bischoff et al., 2013; Roy et al., 2014; Stanganello and Scholpp, 2016). In *Xenopus* embryos, these structures have been reported to align with FN matrix assembled by BCR cells (Boucaut et al., 1990) and to promote cytoplasmic exchange (Danilchik et al., 2013). It is perhaps interesting to note that these specialized filopodia extend into the cleft of Brachet, where they may participate in receptor-mediated signaling important in mesendoderm development. The cleft of Brachet is a fluid-filled compartment defined by the space between the BCR and the involuting mesoderm. It is bounded and possibly 'sealed-off' from the blastocoel cavity by the tightly adherent advancing forward

Development (2017) 144, 4363-4376 doi:10.1242/dev.155200

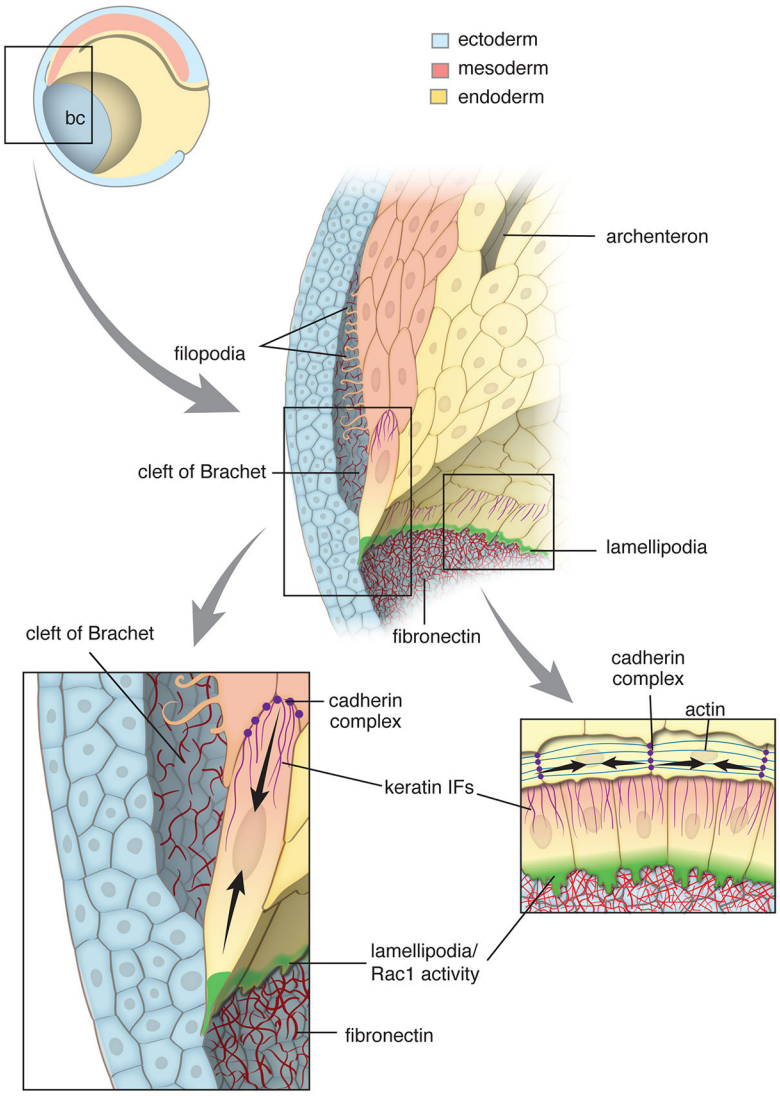

Fig. 7. Summary of mesendoderm morphogenesis in a mid-gastrula stage *Xenopus* embryo. Center: Cut-away profile view of the boxed region from a bisected embryo (upper left; bc, blastocoel) showing the anterior progression of the mesendoderm and its spatial relationship to the BCR, fibrillar FN matrix, and the trailing mesoderm and endoderm. Lower left: Higher magnification view highlighting the leading edge mesendoderm cell with large forward protrusion 'pulling' on the overlying BCR. The FN matrix is remodeled as the leading edge passes over it. The rear of the leading edge cell is attached to follower row cells via a cadherin-containing adhesion complex that includes a basket-like arrangement of keratin filaments. Arrows indicate the balancing of forward traction stresses with intercellular stresses at the rear. Follower cells extend long specialized filopodia (cytonemes) into the cleft of Brachet, which is widened at this location by the failure of following row cells to adhere to the BCR. Lower right: En face view of mesendoderm highlighting the relationship of leading edge cells with their broad lamellipodia in contact with the BCR, to circumferentially arranged upper row cells with their stress fiber-like organization of actin filaments (see also Fig. S6). Upper row cells likely contribute to closure of the mesendoderm mantle by applying tangential stresses (black arrows) perpendicular to the radial stresses of the underlying leading row cells. Rac1 activity gradient (green shading) in leading edge cells is highest in the protrusions.

edge of the mesendodermal mantle (Fig. 7). Plouhinec et al. (2013) reported that chordin secreted by the dorsal Spemann organizer region of the ectoderm diffuses within the cleft to form a morphogen signaling gradient, which raises the intriguing possibility that the observed remodeling of the FN fibrillar matrix by the advancing mesendoderm (Davidson et al., 2004) represents the release of fragments of FN and any associated chemokines (e.g. PDGF) (Smith et al., 2009) into the cleft, where they are then sampled by these filopodia. Leader cells involved in collective cell invasion have been shown to upregulate matrix metalloproteinases and degrade ECM (Gaggioli et al., 2007; Wolf et al., 2007). It will be of interest to establish in future studies if leading edge cells proteolytically modify the FN matrix or, as a result of applied cell traction stresses, cause the force-induced unfolding of FN to expose cryptic binding sites with biological activity (Smith et al., 2007).

A role for the keratin IF cytoskeleton in mesendoderm tissue organization?

Knockdown of keratin IFs dramatically alters follower row cell behaviors, indicating the likely importance of maintaining strong cell-cell adhesions in the tissue to balance leading edge tractions. The functional consequences of reduced keratin levels include increased traction stresses (Fig. 1D) and maturation of FAs (Fig. 3), altered cell protrusions (Fig. 2), and reorganization of the actin cytoskeleton from fine cortical filaments in the cell body to stress fibers (Fig. 4). The overall migration rate of krt8 morphants is also lower (Fig. S3), possibly resulting from lack of FA turnover (Webb et al., 2004). Previously, we reported that local tugging forces on C-cadherins in single mesendoderm cells on FN results in recruitment of keratin IFs, cell repolarization and directed migration (Weber et al., 2012). Keratin IFs are known to provide mechanical integrity to cells (Coulombe et al., 1991; Ramms et al., 2013) and are involved in maintaining strong cellular adhesions (Huen et al., 2002; Kröger et al., 2013). It is likely that keratin IFs are playing a similar role in the mesendoderm.

Thus, we hypothesize that in krt8 morphants, high traction stresses generated at the leading edge are unable to be resisted by weakened cell-cell adhesions in the following rows. This results in increases in cell-ECM adhesion, traction stresses and FA maturation, but because these cells are no longer able to balance the directional forces generated by leading row cells, they become randomly protrusive and misoriented. Similar modulation of cell-ECM traction stresses in response to disruptions in cadherin-based adhesions have been reported for clusters of cultured keratinocytes (Mertz et al., 2013).

Knockdown of krt8 results in a striking reorganization of the actin cytoskeleton and presence of mature FAs in both leading and

Development (2017) 144, 4363-4376 doi:10.1242/dev.155200

following rows of cells. In cultured cells, depletion of plectin, which functions as a linker of actin and intermediate filaments and microtubules, results in increased MAP kinase signaling and enhanced stress fiber formation (Osmanagic-Myers et al., 2006). Although the mechanisms responsible for increased stress fiber formation and contractility in keratin-depleted mesendoderm are not known, it is possible that loss of keratin IFs alters plectin function resulting in global changes in cytoskeletal organization. Significant increases in actin stress fibers noted at mesendoderm cell junctions in keratin morphant cells (Fig. 4H) could also be compensating for the loss of mechanical integrity associated with reduced keratin IFs. Disruptions of desmosomal junctions are associated with increased myosin II levels at adherens junctions, which promotes contractility (Sumigray et al., 2014; Yonemura et al., 1995) and junctional stability (Cavey and Lecuit, 2009).

Cells are able to sense and respond to changes in matrix rigidity during migration, and mysoin II is recruited to reinforce integrin adhesions as substrate forces increase (Choi et al., 2008; Galbraith and Sheetz, 1998). We observed a similar, integrin-dependent increase in mysoin II activity (i.e. pMLC levels) in control mesendoderm cells subject to stretch on FN (Fig. 5). Stretching control cells on C-cad-FC substrates had no effect on mysoin II activity. This might reflect resistance to stretch being borne by keratin IF-based cadherin adhesions. Interestingly, MLC activity is elevated in krt8 morphant cells plated on either FN or C-cad-FC, further suggesting that MLC phosphorylation is upregulated to compensate for loss of mechanical integrity in keratin IF-depleted cells.

Rho GTPases are important regulators of cell adhesions and cytoskeletal networks (Nobes and Hall, 1999), and are subject to tight spatiotemporal regulation in migratory cells (Machacek et al., 2009; Yamada and Nelson, 2007). As reported in other systems, Rac1 activity is highest in lamellipodia, where it spatially coincides with FAs at the leading edge of mesendoderm explants. Disruption of the Rac1 activity gradient in keratin morphants, and the disassembly of keratin IFs resulting from photoactivation of Rac1 (Fig. 6), suggest that keratin IFs may normally antagonize Rac1 activity; for example, at the cell rear, where keratin IFs are assembled in a basket-like arrangement (Weber et al., 2012) (Fig. 7). Similar mechanisms have been reported for vimentin (Helfand et al., 2011; Jiu et al., 2017) and keratin 18 (Fujiwara et al., 2016). The presence of actin stress fibers and increased cell contractility in krt8 morphant cells might thus reflect an upregulation of RhoA signaling (Chrzanowska-Wodnicka and Burridge, 1996). Inhibiting mysoin II activity in krt8 morphant explants with ROCK kinase inhibitor blocks the formation of actin stress fibers and leads to the formation of lamellipodia similar to those of control cells. Overall, we conclude that keratin IFs play an important role in cell migration, possibly by regulating the activities of Rho-GTPase family member proteins.

Geometry of mesendoderm closure

Most of the data reported in this study were obtained using the DMZ explant (Fig. S1). This explant also allows migration movements to be followed for longer periods of time than in the donut (Fig. S1), which ultimately 'closes' coincident with the cessation of cell migration. Although the overall features of mesendoderm migration and organization are shared in both preparations, there are some differences. These include a higher velocity of cell migration in donuts that more closely matches the rate in embryos (Davidson et al., 2002) and a more dynamic, complex pattern of traction stresses along the leading edge (Fig. S2). Average radial traction stresses are not only lower overall but also reveal a dorsal-ventral asymmetry. Mesendoderm migration begins on the dorsal side of the embryo and extends laterally to the ventral side with time. The ventral margins of donut explants fail to generate strong radial tractions, even though the cells continue to move at a rate comparable to cells on the dorsal side of the donut. In the absence of significant ventral radial traction stresses how does closure occur? Donut explants may also generate tangential forces that likely originate in follower row cells that are located above the leader and follower rows that face the BCR (Fig. 7; Fig. S7A-C). Many of these upper follower row (ufr) cells have their long axes oriented perpendicular to the forward-directed leading row cells attached firmly to the BCR FN. Actin stress fibers run the length of these ufr cells terminating at cell junctions, where they appear continuous with stress fibers in neighboring cells (Fig. S7C). We propose that these circumferentially arranged cells are the source of tangential stresses helping to drive closure of the mesendoderm in donut explants and in embryos (Fig. 7), even in the absence of significant radial traction stresses. Future studies will be needed to establish the contribution of ufr cell contractility to closure. The presence of these cells suggests another morphogenetic machine working in concert with leading row traction stresses to shape the mesendoderm and guide its collective movement at gastrulation.

The importance of the keratin IF system as an integrator of mechanical forces required for the multiple morphogenetic movements of *Xenopus* gastrulation was first proposed by Klymkowsky et al. (1992). The current study provides direct evidence for keratin IF involvement in coordinating single cell behaviors to effect a tissue-level movement. We conclude that even a delicate rebalancing of traction forces and intercellular stresses can have profound consequences for cell polarity, cytoskeletal organization and the individual motile behaviors of cells involved in directing the collective movements of a tissue.

MATERIALS AND METHODS

Xenopus embryos and explant preparation

Xenopus embryos were obtained using standard methods and staged according to Nieuwkoop and Faber (1994). DMZ and donut explants were prepared as described previously (Davidson et al., 2002) with the modification that Stage 11 embryos were used (Fig. S1). Glass coverslips for explant imaging were washed with alkaline ethanol solution, flamed and then glued, using Norland optical adhesive 68, to openings drilled with a lathe into the bottom of 35-mm petri dishes. Coverslips were then coated with 300 µl of 5.0 µg/ml bovine plasma FN overnight at 4°C. Coverslips were blocked with 5% bovine serum albumin (BSA) and washed, and dishes were filled with 1× modified Barth's saline (MBS). DMZ explants were plated for 1 h prior to imaging.

Morpholino oligonucleotides

Antisense morpholino oligonucleotides (MO) to inhibit krt8 expression were purchased from GeneTools and injected into the animal pole of embryos immediately after fertilization at a concentration of 40 ng/embryo. The keratin MO (5′-TCGATCTGACGGACATGGTGGAGCT-3′) was designed using *Xenopus* krt8 sequence NCBI accession number NM_00108756.1 (Weber et al., 2012). Control injections used the GeneTools Standard Control MO (5′-CCTCTTACCTCAGTTACAATTTATA-3′).

RNA constructs

RNA encoding fluorescently tagged proteins was transcribed *in vitro* from linearized plasmids. Transcripts were injected into the DMZ region of two blastomeres at the two- or four-cell stage, to a final concentration of 200-2000 pg RNA per embryo (Table 1). The following constructs were used in this study: pCS2+ LifeAct-mCherry (Pfister et al., 2016), pCS2+ α5-GFP (construct was made by cloning EGFP in frame with the cytoplasmic tail of *Xenopus* α5 integrin using Stu1 and Not1), pCS2+ GAP43-EGFP (E. DeRobertis, University of California, Los Angeles, CA, USA), pTriEX

Development (2017) 144, 4363-4376 doi:10.1242/dev.155200

Table 1. RNA transcripts injected

RNA transcript	Picograms injected per embryo
LifeAct-mCherry	250
α5-GFP	250
GAP43-EGFP	200
Rac1 Biosensor	1600-2000
Turquoise Rac1	800-1000
yPet PBD	800-1000
EGFP-paxillin	250
EGFP-krt8	500
mCherry-PA-Rac1Q61L	2000
mCherry-PA-Rac1C450A	2000

Rac1 Biosensor, Turquoise-Rac1 and Ypet-PBD (K. Hahn, University of North Carolina, Chapel Hill, NC, USA) pCS2+ EGFP-paxillin (subcloned by cold fusion into pCS2+ using Xba1 and SnaB1 from a construct obtained from R. Horwitz (University of Virginia, Charlottesville, VA, USA), pCS2+ EGFP-krt8 (V. Allan, University of Manchester, Manchester, UK) (Clarke and Allan, 2003), pTriEx-mCherry-PA-Rac1Q61L and pTriEx mCherry-PA-Rac1C450A (K. Hahn, University of North Carolina).

TFM: preparation of polyacrylamide gels with NHS ester

Polyacrylamide gels with N-hydroxysuccinimide (NHS) ester were prepared using the methods described in Rajagopalan et al. (2004), with a few modifications. In brief, a mixture containing 6% acrylamide (Thermo Fisher Scientific), 0.36% bis-acrylamide (Thermo Fisher Scientific), 15 µmol/ml acrylic acid NHS ester (Thermo Fisher Scientific), 20% 0.25M 4-(2-hydroxyethyl)-1-piperazineethanesulfonic acid (HEPES) (Thermo Fisher Scientific) was made and the pH of the solution was adjusted to 5.9-6.0 by careful addition of 1M HCL. To 250 µl of this solution, ∼50 µl of 1 µm diameter fluorescent beads (Sphero carboxyl fluorescent particles, yellow; 1% w/v) (Spherotech) were added immediately, followed by addition of ammonium persulfate (1% final volume) to initiate polymerization. Before polymerization, the solution was cast on coverslips, which were already activated with 3-3-aminopropyltrimethoxysilane and glutaraldehyde. To ensure that the beads were packed properly, dishes with unpolymerized gel were centrifuged at 900 rpm for 20 min. The elastic modulus of the gel was determined to be 18.4±1.9 kPa by the ball indentation method (Dimitriadis et al., 2002). DMZ or donut explants from embryos injected with Alexa Fluor 555-labeled 10,000 kDa dextran (#D34679, Invitrogen) were plated on polyacrylamide gels embedded with beads. Time-lapse images of fluorescent dextran-filled cells (to visualize cell positions) and fluorescent beads were taken, beginning 1 h after explants were plated. Following imaging, trypsin was added to the dish, explants were allowed to detach, and images of the beads were again acquired as a starting-position reference to calculate traction stresses.

TFM: traction stress calculations using MATLAB

Gel deformations were calculated by quantifying bead displacements using a Particle Image Velocimetry (PIV) ImageJ plugin (Tseng et al., 2012). Measurement noises were subsequently attenuated through a self-adaptive filtering scheme (Huang et al., 2012), and then traction forces were calculated from the magnitude and direction of the substrate deformation utilizing Fourier transform traction cytometry (Butler et al., 2002). Both types of calculation were accomplished using MATLAB (MathWorks). The location of leading edges of DMZ and donut explants were determined manually by imaging fluorescent dextran-filled cells, then equally distanced (10 µm) contours were drawn parallel to the leading edge curvature. The area between adjacent contours was used to create 10-µm wide bins spanning the width of the explant. All of the calculated stress value points (stress values were calculated in 8 µm by 8 µm grids) within a bin were averaged to obtain the values represented in each bar of the kymograph as a function of distance from the DMZ leading edge. To calculate vector values, the traction stress vector was resolved into a horizontal component that is propelling the DMZ from left to right when this horizontal component is positive (pointing left), and a vertical component that is perpendicular to it. The vector sums take the directionality of stress into account and represent only the traction stresses contributing to forward movement of the explant. Absolute values represent the total magnitude of the stress regardless of whether it contributes to or resists the forward movement of the explant.

Microscopy and image analysis

Confocal *Z*-stack images were taken on a Nikon C1 confocal microscope at 0.5-1 µm intervals. For time-lapse movies, images were collected every 2 min for 10-15 min. TIRF microscopy was performed using an Olympus 1X70 inverted TIRF microscope with an Olympus 60×/1.45 NA TIRF objective. Time-lapse images were collected 15 s or 30 s apart for 5 min. Areas of FAs and numbers of FAs per cell were calculated by thresholding the images so that only FAs were saturated and the area of the saturated pixels was counted. DMZ explants expressing pCS2+ GAP43-EGFP were used to analyze the length of specialized filopodia and persistence of protrusion. Lengths were measured manually by tracing individual filopodia. Four randomly selected filopodia were measured per cell. Persistence of protrusion was calculated by tracking the number of times an individual protrusion retracts or newly appears over the course of 5 min. Mann–Whitney test was used to determine statistical significance among FA areas, length of specialized filopodia under different conditions and persistence of protrusion.

FRET microscopy

DMZ explants expressing Rac1 Biosensor, Turquoise-Rac1 and Ypet-PBD were imaged using a Leica confocal microscope. While imaging, microscope settings such as laser power and gain were kept constant. FRET efficiency was calculated using the PFRET ImageJ plugin (Chen and Periasamy, 2006) obtained from UVA Keck Center for Cellular Imaging. Line scan profiles of single cells were obtained from FRET efficiency images, and an average of the FRET efficiency was plotted over distance from the front of the cell.

Photoactivation of Rac1

Mesendoderm tissue expressing mCherry-PA-Rac1 constructs (i.e. mCherry-PA Rac1C450A; mCherry-PA Rac1Q61L) and EGFP-keratin was excised at stage 11 and incubated in 1× Ca^{2+}/Mg^{2+}-free MBS (CMF-MBS) to dissociate the cells. Cells were then plated subconfluently onto coverslips coated with FN (10 µg/ml). Cells were allowed to adhere for 1 h and then imaged using a Zeiss Cell Observer SD (spinning disk confocal microscope) with Plan-Apochromat/63× or 100× objectives. A small region of the cells was irradiated with a 457 nm laser using a Zeiss Direct FRAP manipulation add-on hardware module. Statistical significance was determined using Student's *t*-test at each time point condition. Independent confirmation of these results was obtained in a separate set of experiments using an Olympus FV1000 with UPlanSApo/60×/1.35 NA objective (number of cells analyzed with the Olympus confocal microscope: eGFP-PA Rac1C450A=six cells across three independent experiments; eGFP-PA Rac1Q61L=nine cells across seven independent experiments). Data obtained with the Zeiss system are included in Fig. 6F-L.

Explant treatment, fixation and actin staining

DMZ explants on FN were treated with DMSO or 10 µM Y27632, 5 mM acrylamide or 10 mM acrylamide for 1 h. DMZ explants were fixed in 0.25% glutaraldehyde, 3.7% formaldehyde and 0.1% Tween 20 for 10 min at room temperature, stained with 488-ActiStain (Cytoskeleton) and imaged with a Nikon C1 confocal microscope.

Removal of leading edge cells from DMZ explants

DMZ explants expressing EGFP-paxillin and LifeAct-mCherry were plated on coverslips coated with FN (5 µg/ml). Explants were allowed to adhere for 1 h and imaged on an Olympus 1×70 inverted TIRF microscope with an Olympus 60×/1.45 NA TIRF objective. The leading edge of the explant was carefully excised using an eyebrow knife and allowed to heal for 1 h, before images of the explants were taken again on the same microscope.

Scanning electron microscopy

Stage 11.5 *Xenopus* gastrula were fixed overnight with 4% formaldehyde/2.5% glutaraldehyde in 0.1× MBS. The BCR was removed from fixed embryos to expose the basal side of the mesendoderm tissue. Samples were

Development (2017) 144, 4363-4376 doi:10.1242/dev.155200

postfixed in 1% OsO_4, critical-point dried, and gold-palladium sputter coated. Specimens were imaged using a Zeiss Sigma VP HD Field Scanning Electron Microscope.

Cell stretching and pMLC western blot analysis

Whole mesendoderm tissue from control and krt8 MO-injected embryos was dissected and dissociated in 1× CMF-MBS. Dissociated cells were then plated in a silicone well plate (Cell Scale) previously coated overnight at 4°C with 200 µl of 10 µg/ml FN or C-cad-Fc. Wells were blocked with 5% BSA, then washed and filled with 100 µl of 1× MBS. Cells were allowed to adhere for 1 h before the membranes were cyclically stretched (10% stretch) using a MechanoCulture FX stretching device (Cell Scale). Fifteen cycles of 10 s stretch, 10 s hold, 10 s relax and 10 s hold were performed. Some cells were kept in 1× CMF-MBS in suspension for the duration of the stretch cycles to serve as nonadherent controls. Cells were lysed with 100 µl lysis buffer [100 mM NaCl, 25 mM Tris HCl pH7.4, 1 mM EDTA, 1 mM EGTA, 1 mM beta-glycerophosphate, 2.5 mM $Na_4P_2O_7$, 1% NP40, protease inhibitor cocktail (P2714, Sigma-Aldrich) and 1 mM PMSF]. Cell lysates were centrifuged for 10 min at 14,000 rpm at 4°C to remove yolk. The supernatants were transferred to new tubes, diluted with 6× reducing Laemmli buffer, separated by SDS-PAGE (10% or 12%) and transferred onto nitrocellulose membranes. Blots were probed with antibodies directed against pMLC (S19; 3671, Cell Signaling Technology; 1:1000 dilution) and beta-actin (A3854, Sigma-Aldrich; 1:25,000 dilution). Signal intensity for each band was quantified using ImageJ and ratios of pMLC to beta-actin were calculated in Microsoft Excel. Paired Student's *t*-test was used to evaluate statistical differences in pMLC levels under different conditions.

Acknowledgements

We thank Klaus Hahn at the University of North Carolina for the Rac1 FRET and Rac1 photoinducible constructs; members of the W. M. Keck Center for Cellular Imaging at the University of Virginia for assistance with TIRF, FRET imaging and data analysis; and Rick Horwitz for advice related to the Rac1 GTPase photoactivation experiments. We are grateful to Karen Litwa, Ryan D'Souza, and the current and past members of the DeSimone laboratory for helpful discussions and technical advice over the course of this study. We also thank Anita Impagliazzo for the artwork presented in Fig. 7.

Competing interests

The authors declare no competing or financial interests.

Author contributions

Conceptualization: P.R.S., C.W., B.D., G.F.W., D.W.D.; Methodology: P.R.S., C.W., B.D., G.F.W., A.P.; Software: C.W.; Validation: P.R.S., B.D.; Investigation: B.D., D.W.D.; Resources: D.W.D.; Writing - original draft: P.R.S., D.W.D.; Writing - review & editing: C.W., B.D., G.F.W., D.W.D.; Supervision: D.W.D.; Funding acquisition: D.W.D.

Funding

This work was supported by the Office of Extramural Research, National Institutes of Health [GM094793 to D.W.D. and HD084254 to G.F.W.]. Deposited in PMC for release after 12 months.

Supplementary information

Supplementary information available online at
http://dev.biologists.org/lookup/doi/10.1242/dev.155200.supplemental

References

Beningo, K. A., Dembo, M., Kaverina, I., Small, J. V. and Wang, Y.-L. (2001). Nascent focal adhesions are responsible for the generation of strong propulsive forces in migrating fibroblasts. *J. Cell Biol.* **153**, 881-888.

Bischoff, M., Gradilla, A.-C., Seijo, I., Andrés, G., Rodríguez-Navas, C., González-Méndez, L. and Guerrero, I. (2013). Cytonemes are required for the establishment of a normal Hedgehog morphogen gradient in Drosophila epithelia. *Nat. Cell Biol.* **15**, 1269-1281.

Bjerke, M. A., Dzamba, B. J., Wang, C. and DeSimone, D. W. (2014). FAK is required for tension-dependent organization of collective cell movements in Xenopus mesendoderm. *Dev. Biol.* **394**, 340-356.

Borghi, N., Lowndes, M., Maruthamuthu, V., Gardel, M. L. and Nelson, W. J. (2010). Regulation of cell motile behavior by crosstalk between cadherin- and integrin-mediated adhesions. *Proc. Natl. Acad. Sci. USA* **107**, 13324-13329.

Boucaut, J. C., Johnson, K. E., Darribère, T., Shi, D. L., Riou, J. F., Bache, H. B. and Delarue, M. (1990). Fibronectin-rich fibrillar extracellular matrix controls cell migration during amphibian gastrulation. *Int. J. Dev. Biol.* **34**, 139-147.

Brugues, A., Anon, E., Conte, V., Veldhuis, J. H., Gupta, M., Colombelli, J., Muñoz, J. J., Brodland, G. W., Ladoux, B. and Trepat, X. (2014). Forces driving epithelial wound healing. *Nat. Phys.* **10**, 683-690.

Butler, J. P., Tolić-Nørrelykke, I. M., Fabry, B. and Fredberg, J. J. (2002). Traction fields, moments, and strain energy that cells exert on their surroundings. *Am. J. Physiol. Cell Physiol.* **282**, C595-C605.

Cai, D., Chen, S.-C., Prasad, M., He, L., Wang, X., Choesmel-Cadamuro, V., Sawyer, J. K., Danuser, G. and Montell, D. J. (2014). Mechanical feedback through E-cadherin promotes direction sensing during collective cell migration. *Cell* **157**, 1146-1159.

Caussinus, E., Colombelli, J. and Affolter, M. (2008). Tip-cell migration controls stalk-cell intercalation during Drosophila tracheal tube elongation. *Curr. Biol.* **18**, 1727-1734.

Cavey, M. and Lecuit, T. (2009). Molecular bases of cell-cell junctions stability and dynamics. *Cold Spring Harbor Perspect. Biol.* **1**, a002998-a002998.

Chen, Y. and Periasamy, A. (2006). Intensity range based quantitative FRET data analysis to localize protein molecules in live cell nuclei. *J. Fluoresc.* **16**, 95-104.

Cheung, K. J., Gabrielson, E., Werb, Z. and Ewald, A. J. (2013). Collective invasion in breast cancer requires a conserved basal epithelial program. *Cell* **155**, 1639-1651.

Cheung, K. J., Padmanaban, V., Silvestri, V., Schipper, K., Cohen, J. D., Fairchild, A. N., Gorin, M. A., Verdone, J. E., Pienta, K. J., Bader, J. S. et al. (2016). Polyclonal breast cancer metastases arise from collective dissemination of keratin 14-expressing tumor cell clusters. *Proc. Natl. Acad. Sci. USA* **113**, E854-E863.

Choi, C. K., Vicente-Manzanares, M., Zareno, J., Whitmore, L. A., Mogilner, A. and Horwitz, A. R. (2008). Actin and |[alpha]|-actinin orchestrate the assembly and maturation of nascent adhesions in a myosin II motor-independent manner. *Nat. Cell Biol.* **10**, 1039-1050.

Chrzanowska-Wodnicka, M. and Burridge, K. (1996). Rho-stimulated contractility drives the formation of stress fibers and focal adhesions. *J. Cell Biol.* **133**, 1403-1415.

Clark, K., Langeslag, M., Figdor, C. G. and van Leeuwen, F. N. (2007). Myosin II and mechanotransduction: a balancing act. *Trends Cell Biol.* **17**, 178-186.

Clarke, E. J. and Allan, V. J. (2003). Cytokeratin intermediate filament organisation and dynamics in the vegetal cortex of living Xenopus laevis oocytes and eggs. *Cell Motil. Cytoskeleton* **56**, 13-26.

Collins, C. and Nelson, W. J. (2015). Running with neighbors: coordinating cell migration and cell–cell adhesion. *Curr. Opin. Cell Biol.* **36**, 62-70.

Coulombe, P. A., Hutton, M. E., Vassar, R. and Fuchs, E. (1991). A function for keratins and a common thread among different types of epidermolysis bullosa simplex diseases. *J. Cell Biol.* **115**, 1661-1674.

Danilchik, M., Williams, M. and Brown, E. (2013). Blastocoel-spanning filopodia in cleavage-stage Xenopus laevis: Potential roles in morphogen distribution and detection. *Dev. Biol.* **382**, 70-81.

Das, T., Safferling, K., Rausch, S., Grabe, N., Boehm, H. and Spatz, J. P. (2015). A molecular mechanotransduction pathway regulates collective migration of epithelial cells. *Nat. Cell Biol.* **17**, 276-287.

Davidson, L. A., Hoffstrom, B. G., Keller, R. and DeSimone, D. W. (2002). Mesendoderm extension and mantle closure in Xenopus laevis gastrulation: combined roles for integrin alpha(5)beta(1), fibronectin, and tissue geometry. *Dev. Biol.* **242**, 109-129.

Davidson, L. A., Keller, R. and DeSimone, D. W. (2004). Assembly and remodeling of the fibrillar fibronectin extracellular matrix during gastrulation and neurulation in Xenopus laevis. *Dev. Dynam.* **231**, 888-895.

Del Pozo, M. A., Kiosses, W. B., Alderson, N. B., Meller, N., Hahn, K. M. and Schwartz, M. A. (2002). Integrins regulate GTP-Rac localized effector interactions through dissociation of Rho-GDI. *Nat. Cell Biol.* **4**, 232-239.

Dimitriadis, E. K., Horkay, F., Maresca, J., Kachar, B. and Chadwick, R. S. (2002). Determination of elastic moduli of thin layers of soft material using the atomic force microscope. *Biophys. J.* **82**, 2798-2810.

Dumortier, J. G., Martin, S. and Meyer, D. (2012). Collective mesendoderm migration relies on an intrinsic directionality signal transmitted through cell contacts. *Proc. Natl. Acad. Sci. USA* **109**, 16945-16950.

du Roure, O., Saez, A., Buguin, A., Austin, R. H., Chavrier, P., Silberzan, P., Siberzan, P. and Ladoux, B. (2005). Force mapping in epithelial cell migration. *Proc. Natl Acad. Sci. USA* **102**, 2390-2395.

Eckert, B. S. and Yeagle, P. L. (1988). Acrylamide treatment of PtKI cells causes dephosphorylation of keratin polypeptides. *Cell Motil. Cytoskeleton* **11**, 24-30.

Even-Ram, S., Doyle, A. D., Conti, M. A., Matsumoto, K., Adelstein, R. S. and Yamada, K. M. (2007). Myosin IIA regulates cell motility and actomyosin|[ndash]| microtubule crosstalk. *Nat. Cell Biol.* **9**, 299-309.

Farooqui, R. and Fenteany, G. (2005). Multiple rows of cells behind an epithelial wound edge extend cryptic lamellipodia to collectively drive cell-sheet movement. *J. Cell Sci.* **118**, 51-63.

Franz, J. K. and Franke, W. W. (1986). Cloning of cDNA and amino acid sequence of a cytokeratin expressed in oocytes of Xenopus laevis. *Proc. Natl Acad. Sci. USA* **83**, 6475-6479.
Franz, J. K., Gall, L., Williams, M. A., Picheral, B. and Franke, W. W. (1983). Intermediate-size filaments in a germ cell: Expression of cytokeratins in oocytes and eggs of the frog Xenopus. *Proc. Natl Acad. Sci. USA* **80**, 6254-6258.
Friedl, P. and Gilmour, D. (2009). Collective cell migration in morphogenesis, regeneration and cancer. *Nat. Rev. Mol. Cell Biol.* **10**, 445-457.
Fujiwara, S., Ohashi, K., Mashiko, T., Kondo, H. and Mizuno, K. (2016). Interplay between Solo and keratin filaments is crucial for mechanical force-induced stress fiber reinforcement. *Mol. Biol. Cell* **27**, 954-966.
Gaggioli, C., Hooper, S., Hidalgo-Carcedo, C., Grosse, R., Marshall, J. F., Harrington, K. and Sahai, E. (2007). Fibroblast-led collective invasion of carcinoma cells with differing roles for RhoGTPases in leading and following cells. *Nat. Cell Biol.* **9**, 1392-1400.
Galbraith, C. G. and Sheetz, M. P. (1998). Forces on adhesive contacts affect cell function. *Curr. Opin. Cell Biol.* **10**, 566-571.
Haas, P. and Gilmour, D. (2006). Chemokine signaling mediates self-organizing tissue migration in the zebrafish lateral line. *Dev. Cell* **10**, 673-680.
Heisenberg, C.-P. and Bellaïche, Y. (2013). Forces in tissue morphogenesis and patterning. *Cell* **153**, 948-962.
Helfand, B. T., Mendez, M. G., Murthy, S. N. P., Shumaker, D. K., Grin, B., Mahammad, S., Aebi, U., Wedig, T., Wu, Y. I., Hahn, K. M. et al. (2011). Vimentin organization modulates the formation of lamellipodia. *Mol. Biol. Cell* **22**, 1274-1289.
Hodgson, L., Shen, F. and Hahn, K. (2001). *Biosensors for Characterizing the Dynamics of Rho Family GTPases in Living Cells*. Hoboken: John Wiley & Sons, Inc.
Huang, J., Deng, H., Peng, X., Li, S., Xiong, C. and Fang, J. (2012). Cellular traction force reconstruction based on a self-adaptive filtering scheme. *Cell Mol. Bioeng.* **5**, 205-216.
Huen, A. C., Park, J. K., Godsel, L. M., Chen, X., Bannon, L. J., Amargo, E. V., Hudson, T. Y., Mongiu, A. K., Leigh, I. M., Kelsell, D. P. et al. (2002). Intermediate filament-membrane attachments function synergistically with actin-dependent contacts to regulate intercellular adhesive strength. *J. Cell Biol.* **159**, 1005-1017.
Inaki, M., Vishnu, S., Cliffe, A. and Rørth, P. (2012). Effective guidance of collective migration based on differences in cell states. *Proc. Natl Acad. Sci. USA* **109**, 2027-2032.
Jiu, Y., Peränen, J., Schaible, N., Cheng, F., Eriksson, J. E., Krishnan, R. and Lappalainen, P. (2017). Vimentin intermediate filaments control actin stress fiber assembly through GEF-H1 and RhoA. *J. Cell Sci.* **130**, 892-902.
Klymkowsky, M. W., Shook, D. R. and Maynell, L. A. (1992). Evidence that the deep keratin filament systems of the Xenopus embryo act to ensure normal gastrulation. *Proc. Natl Acad. Sci. USA* **89**, 8736-8740.
Kröger, C., Loschke, F., Schwarz, N., Windoffer, R., Leube, R. E. and Magin, T. M. (2013). Keratins control intercellular adhesion involving PKC-α-mediated desmoplakin phosphorylation. *J. Cell Biol.* **201**, 681-692.
Lauffenburger, D. A. and Horwitz, A. F. (1996). Cell migration: a physically integrated molecular process. *Cell* **84**, 359-369.
Machacek, M., Hodgson, L., Welch, C., Elliott, H., Pertz, O., Nalbant, P., Abell, A., Johnson, G. L., Hahn, K. M. and Danuser, G. (2009). Coordination of Rho GTPase activities during cell protrusion. *Nature* **461**, 99-103.
Malet-Engra, G., Yu, W., Oldani, A., Rey-Barroso, J., Gov, N. S., Scita, G. and Dupré, L. (2015). Collective cell motility promotes chemotactic prowess and resistance to chemorepulsion. *Curr. Biol.* **25**, 242-250.
Mammoto, T., Mammoto, A. and Ingber, D. E. (2013). Mechanobiology and developmental control. *Annu. Rev. Cell Dev. Biol.* **29**, 27-61.
Mayor, R. and Etienne-Manneville, S. (2016). The front and rear of collective cell migration. *Nat. Rev. Mol. Cell Biol.* **17**, 97-109.
Mertz, A. F., Che, Y., Banerjee, S., Goldstein, J. M., Rosowski, K. A., Revilla, S. F., Niessen, C. M., Marchetti, M. C., Dufresne, E. R. and Horsley, V. (2013). Cadherin-based intercellular adhesions organize epithelial cell–matrix traction forces. *Proc. Natl Acad. Sci. USA* **110**, 842-847.
Miller, C. J. and Davidson, L. A. (2013). The interplay between cell signalling and mechanics in developmental processes. *Nat. Rev. Genet.* **14**, 733-744.
Moosmann, J., Ershov, A., Altapova, V., Baumbach, T., Prasad, M. S., LaBonne, C., Xiao, X., Kashef, J. and Hofmann, R. (2013). X-ray phase-contrast in vivo microtomography probes new aspects of Xenopus gastrulation. *Nature* **497**, 374-377.
Nieuwkoop, P. D. and Faber, J. (1994). *Normal Table of Xenopus Laevis (Daudin)*. New York, NY: Garland.
Nobes, C. D. and Hall, A. (1999). Rho GTPases control polarity, protrusion, and adhesion during cell movement. *J. Cell Biol.* **144**, 1235-1244.
Nogare, D. D., Somers, K., Rao, S. and Matsuda, M. (2014). Leading and trailing cells cooperate in collective migration of the zebrafish posterior lateral line primordium. *Development* **141**, 3188-3196.
Osmanagic-Myers, S., Gregor, M., Walko, G., Burgstaller, G., Reipert, S. and Wiche, G. (2006). Plectin-controlled keratin cytoarchitecture affects MAP kinases involved in cellular stress response and migration. *J. Cell Biol.* **174**, 557-568.
Pasapera, A. M., Schneider, I. C., Rericha, E., Schlaepfer, D. D. and Waterman, C. M. (2010). Myosin II activity regulates vinculin recruitment to focal adhesions through FAK-mediated paxillin phosphorylation. *J. Cell Biol.* **188**, 877-890.
Pfister, K., Shook, D. R., Chang, C., Keller, R. and Skoglund, P. (2016). Molecular model for force production and transmission during vertebrate gastrulation. *Development* **143**, 715-727.
Plotnikov, S. V., Pasapera, A. M., Sabass, B. and Waterman, C. M. (2012). Force fluctuations within focal adhesions mediate ECM-rigidity sensing to guide directed cell migration. *Cell* **151**, 1513-1527.
Plouhinec, J.-L., Zakin, L., Moriyama, Y. and De Robertis, E. M. (2013). Chordin forms a self-organizing morphogen gradient in the extracellular space between ectoderm and mesoderm in the Xenopus embryo. *Proc. Natl Acad. Sci. USA* **110**, 20372-20379.
Rajagopalan, P., Marganski, W. A., Brown, X. Q. and Wong, J. Y. (2004). Direct comparison of the spread area, contractility, and migration of balb/c 3T3 fibroblasts adhered to fibronectin- and RGD-modified substrata. *Biophys. J.* **87**, 2818-2827.
Ramms, L., Fabris, G., Windoffer, R., Schwarz, N., Springer, R., Zhou, C., Lazar, J., Stiefel, S., Hersch, N., Schnakenberg, U. et al. (2013). Keratins as the main component for the mechanical integrity of keratinocytes. *Proc. Natl Acad. Sci. USA* **110**, 18513-18518.
Rausch, S., Das, T., Soiné, J. R. D., Hofmann, T. W., Boehm, C. H. J., Schwarz, U. S., Boehm, H. and Spatz, J. P. (2013). Polarizing cytoskeletal tension to induce leader cell formation during collective cell migration. *Biointerphases* **8**, 32.
Reffay, M., Parrini, M. C., Cochet-Escartin, O., Ladoux, B., Buguin, A., Coscoy, S., Amblard, F., Camonis, J. and Silberzan, P. (2014). Interplay of RhoA and mechanical forces in collective cell migration driven by leader cells. *Nat. Cell Biol.* **16**, 217-223.
Ridley, A. J. (2015). Rho GTPase signalling in cell migration. *Curr. Opin. Cell Biol.* **36**, 103-112.
Ridley, A. J., Paterson, H. F., Johnston, C. L., Diekmann, D. and Hall, A. (1992). The small GTP-binding protein rac regulates growth factor-induced membrane ruffling. *Cell* **70**, 401-410.
Riedl, J., Crevenna, A. H., Kessenbrock, K., Yu, J. H., Neukirchen, D., Bista, M., Bradke, F., Jenne, D., Holak, T. A., Werb, Z. et al. (2008). Lifeact: a versatile marker to visualize F-actin. *Nat. Methods* **5**, 605-607.
Roca-Cusachs, P., del Rio, A., Puklin-Faucher, E., Gauthier, N. C., Biais, N. and Sheetz, M. P. (2013). Integrin-dependent force transmission to the extracellular matrix by α-actinin triggers adhesion maturation. *Proc. Natl Acad. Sci. USA* **110**, E1361-E1370.
Roy, S., Huang, H., Liu, S. and Kornberg, T. B. (2014). Cytoneme-mediated contact-dependent transport of the drosophila decapentaplegic signaling protein. *Science* **343**, 1244624-1244624.
Smith, M. L., Gourdon, D., Little, W. C., Kubow, K. E., Eguiluz, R. A., Luna-Morris, S. and Vogel, V. (2007). Force-induced unfolding of fibronectin in the extracellular matrix of living cells. *PLoS Biol.* **5**, e268.
Smith, E. M., Mitsi, M., Nugent, M. A. and Symes, K. (2009). PDGF-A interactions with fibronectin reveal a critical role for heparan sulfate in directed cell migration during Xenopus gastrulation. *Proc. Natl Acad. Sci. USA* **106**, 21683-21688.
Stanganello, E. and Scholpp, S. (2016). Role of cytonemes in Wnt transport. *J. Cell Sci.* **129**, 665-672.
Sumigray, K., Zhou, K. and Lechler, T. (2014). Cell-cell adhesions and cell contractility are upregulated upon desmosome disruption. *PLoS ONE* **9**, e101824.
Tambe, D. T., Hardin, C. C., Angelini, T. E., Rajendran, K., Park, C. Y., Serra-Picamal, X., Zhou, E. H., Zaman, M. H., Butler, J. P., Weitz, D. A. et al. (2011). Collective cell guidance by cooperative intercellular forces. *Nat. Mater.* **10**, 469-475.
Theveneau, E., Marchant, L., Kuriyama, S., Gull, M., Moepps, B., Parsons, M. and Mayor, R. (2010). Collective chemotaxis requires contact-dependent cell polarity. *Dev. Cell* **19**, 39-53.
Trepat, X., Wasserman, M. R., Angelini, T. E., Millet, E., Weitz, D. A., Butler, J. P. and Fredberg, J. J. (2009). Physical forces during collective cell migration. *Nat. Phys.* **5**, 426-430.
Tse, J. M., Cheng, G., Tyrrell, J. A., Wilcox-Adelman, S. A., Boucher, Y., Jain, R. K. and Munn, L. L. (2012). Mechanical compression drives cancer cells toward invasive phenotype. *Proc. Natl Acad. Sci. USA* **109**, 911-916.
Tseng, Q., Duchemin-Pelletier, E., Deshiere, A., Balland, M., Guillou, H., Filhol, O. and Théry, M. (2012). Spatial organization of the extracellular matrix regulates cell-cell junction positioning. *Proc. Natl Acad. Sci. USA* **109**, 1506-1511.
Turner, C. E. (2000). Paxillin and focal adhesion signalling. *Nat. Cell Biol.* **2**, E231-E236.
Valgeirsdóttir, S., Claesson-Welsh, L., Bongcam-Rudloff, E., Hellman, U., Westermark, B. and Heldin, C. H. (1998). PDGF induces reorganization of vimentin filaments. *J. Cell Sci.* **111**, 1973-1980.
Vicente-Manzanares, M., Ma, X., Adelstein, R. S. and Horwitz, A. R. (2009). Non-muscle myosin II takes centre stage in cell adhesion and migration. *Nat. Rev. Mol. Cell Biol.* **10**, 778-790.
Wang, X., He, L., Wu, Y. I., Hahn, K. M. and Montell, D. J. (2010). Light-mediated activation reveals a key role for Rac in collective guidance of cell movement in vivo. *Nat. Cell Biol.* **12**, 591-597.

Development (2017) 144, 4363-4376 doi:10.1242/dev.155200

Webb, D. J., Donais, K., Whitmore, L. A., Thomas, S. M., Turner, C. E., Parsons, J. T. and Horwitz, A. F. (2004). FAK–Src signalling through paxillin, ERK and MLCK regulates adhesion disassembly. *Nat. Cell Biol.* **6**, 154-161.

Weber, G. F., Bjerke, M. A. and DeSimone, D. W. (2012). A mechanoresponsive cadherin-keratin complex directs polarized protrusive behavior and collective cell migration. *Dev. Cell* **22**, 104-115.

Winklbauer, R. and Nagel, M. (1991). Directional mesoderm cell migration in the Xenopus gastrula. *Dev. Biol.* **148**, 573-589.

Winklbauer, R. and Selchow, A. (1992). Motile behavior and protrusive activity of migratory mesoderm cells from the Xenopus gastrula. *Dev. Biol.* **150**, 335-351.

Wolf, K., Wu, Y. I., Liu, Y., Geiger, J., Tam, E., Overall, C., Stack, M. S. and Friedl, P. (2007). Multi-step pericellular proteolysis controls the transition from individual to collective cancer cell invasion. *Nat. Cell Biol.* **9**, 893-904.

Wozniak, M. A. and Chen, C. S. (2009). Mechanotransduction in development: a growing role for contractility. *Nat. Rev. Mol. Cell Biol.* **10**, 34-43.

Wu, Y. I., Frey, D., Lungu, O. I., Jaehrig, A., Schlichting, I., Kuhlman, B. and Hahn, K. M. (2009). A genetically encoded photoactivatable Rac controls the motility of living cells. *Nature* **461**, 104-108.

Yamada, S. and Nelson, W. J. (2007). Localized zones of Rho and Rac activities drive initiation and expansion of epithelial cell-cell adhesion. *J. Cell Biol.* **178**, 517-527.

Yamaguchi, N., Mizutani, T., Kawabata, K. and Haga, H. (2015). Leader cells regulate collective cell migration via Rac activation in the downstream signaling of integrin β1 and PI3K. *Sci. Rep.* **5**, 7656.

Yonemura, S., Itoh, M., Nagafuchi, A. and Tsukita, S. (1995). Cell-to-cell adherens junction formation and actin filament organization: similarities and differences between non-polarized fibroblasts and polarized epithelial cells. *J. Cell Sci.* **108**, 127-142.

Supplementary Information

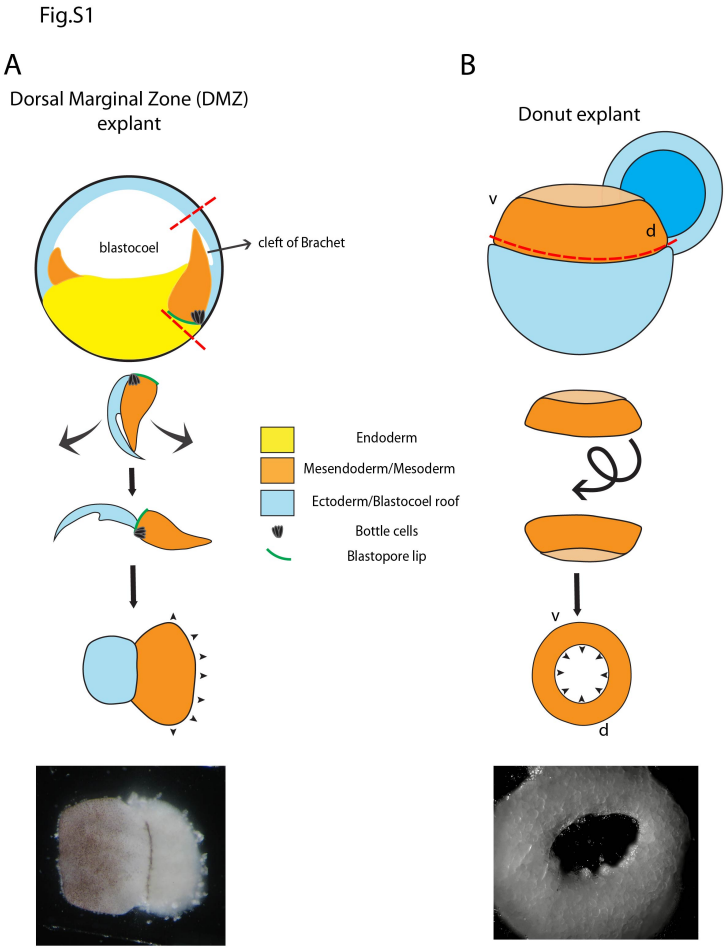

Fig. S1: Preparation of *ex vivo* explants from live embryos.

(A) Cartoon of a bisected stage 11 embryo and steps involved in preparing a Dorsal Marginal Zone (DMZ) explant. Red dashed lines indicate the region of excision. After excision, endoderm tissue adjoining the mesendoderm/mesoderm tissue is removed. The explant is then jackknifed open so that the region normally adjacent to the bcr is placed in contact with a FN coated coverslip. (B) Cartoon of a late stage 11 embryo with blastocoel roof removed to reveal mesendoderm cup. Red dashed line indicates the region of excision. In order to maintain proper orientation with respect to bcr and assembled FN, the donut explant is inverted and placed in contact with a FN coated coverslip. 'd' and 'v' indicate the dorsal and ventral sides of the donut respectively.

Fig.S2

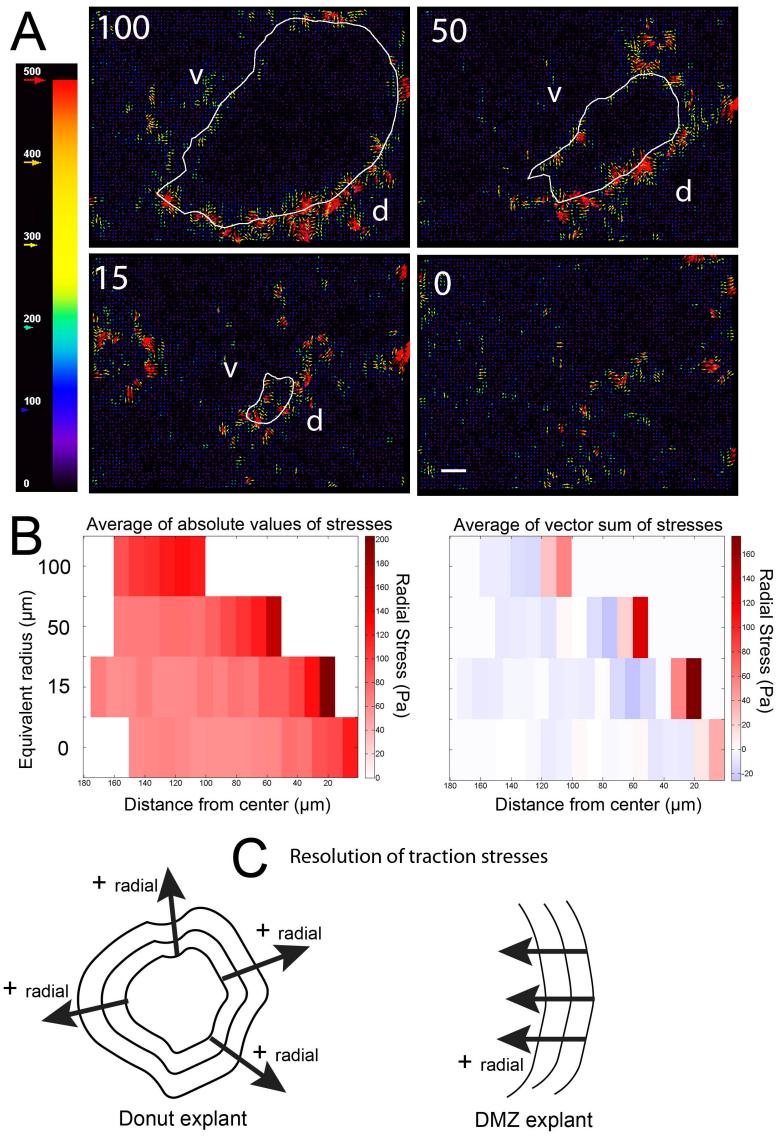

Fig. S2: Traction stresses concentrated at the leading of a donut explant gradually increase as the donut closes.

(A) Representative traction stress maps of a control donut explant at four stages of closure. Arrows in the heat map indicate directions of force and are scaled and pseudocolored to indicate force magnitude. White lines on the maps correspond to the leading edge of the donut and show the progression of donut closure over time. Numbers on each panel indicate the equivalent radii of open area in center of the donut. Equivalent radii were derived from the area of the open center (Area=Πr^2). 'd' and 'v' indicate the dorsal and ventral sides of the donut respectively. Scale bar =25µm. (B) Kymographs of average traction stress generated by mesendoderm cells during donut closure. The donut explant

was divided into 10μm wide concentric contours from the leading edge and mean traction stresses within each 10μm region were calculated. The X-axis of the kymograph represents the distance from the donut center and the Y-axis represents equivalent radii of the donut explant. (C) Cartoon showing resolution of traction stresses in a donut and DMZ explant. For a donut explant, traction stresses perpendicular to the leading edge and opposite to the direction of migration were considered positive radial traction stresses. For a DMZ explant, traction stresses opposite to the direction of migration (left to right) were considered positive radial traction stresses.

Fig.S3

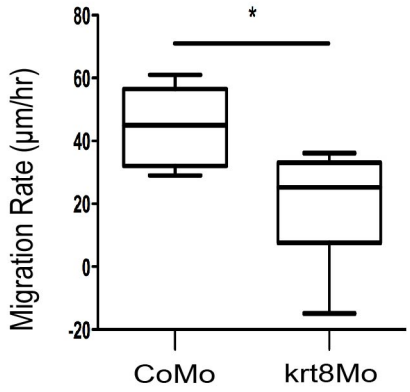

Fig. S3: Migration rates of mesendoderm tissue from control and krt8 morphant embryos.

Positive values denote forward migration and negative values indicate leading edge retractions during the course of migration. Average rate of forward migration for Control Mo: 44.67± 5.077µm/hr and Xck Mo: 19.73± 7.561 µm/hr, * $p<0.05$. Velocities were calculated from two time points from three separate control and krt8 morphant explants.

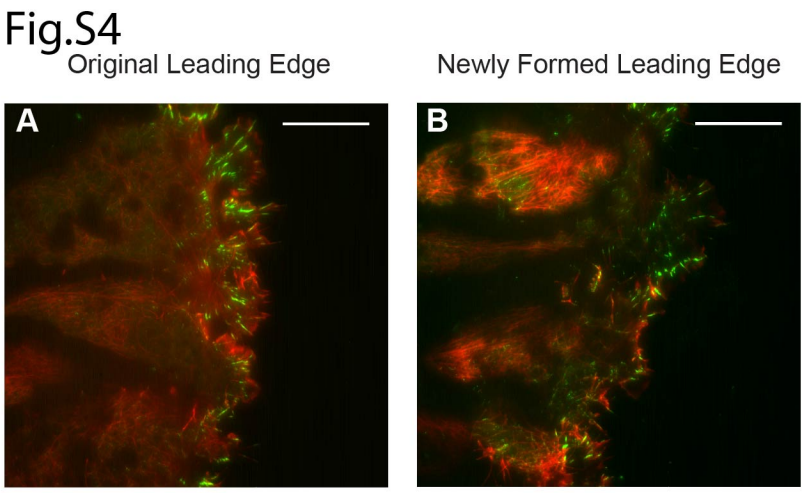

Fig. S4: Following row cells can reorganize to form leading edge cells.

(A) Mesendoderm explant expressing EGFP-paxillin (Green) and LifeAct-mCherry (Red) plated on FN and imaged after one hour using TIRF microscopy. The leading edge of the explant was excised with an eyebrow knife and the explant was allowed to heal for one hour. (B) Following healing, the explant was further imaged (Representative of 4 individual explants across 2 separate experiments). Scale bar=25um (A and B).

Fig.S5

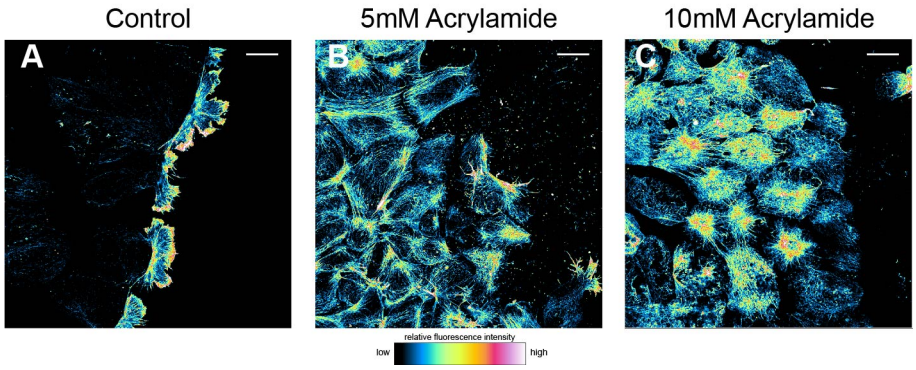

Fig. S5: Acrylamide treatment of mesendoderm explants leads to rearrangement of actin cytoskeleton. (A-C) Confocal projections of fixed and phalloidin stained mesendoderm explants on FN substrates after treatment with acrylamide at the concentrations indicated (B and C). Pseudocolors correspond to the fluorescence intensity heat map (Representative of 9 individual explants per condition imaged across 3 separate experiments). Scale bar=25um (A-C).

Fig.S6

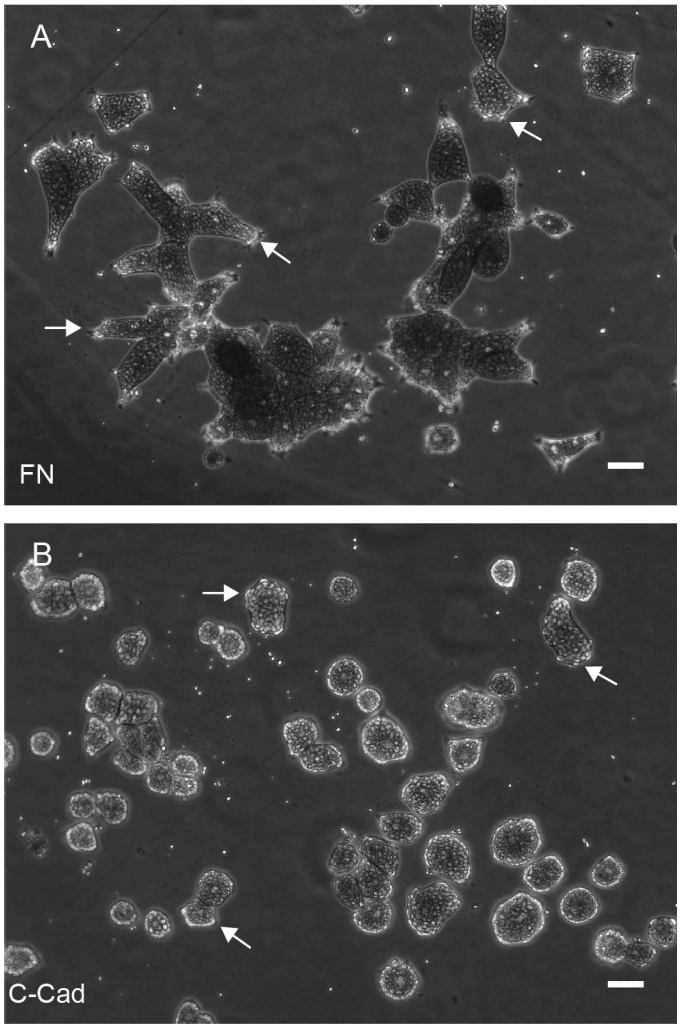

Fig. S6: Mesendoderm Cell morphology on FN and C-cad-FC substrates. (A-B) Representative images of dissociated mesendoderm cells plated on plastic dishes coated with (A) 10µg/ml FN and (B) 5µg/ml C-Cad-FC. After 1 hour, many of these cells have made contact and form small clusters. The morphology of these cells is similar to that observed on stretchable silicon substrates (e.g., Fig. 5A-D) but images of cells on coated plastic substrates are shown here because of the better optical quality. Protrusions are indicated by arrows. Scale bar=50um (A-B).

Fig.S7

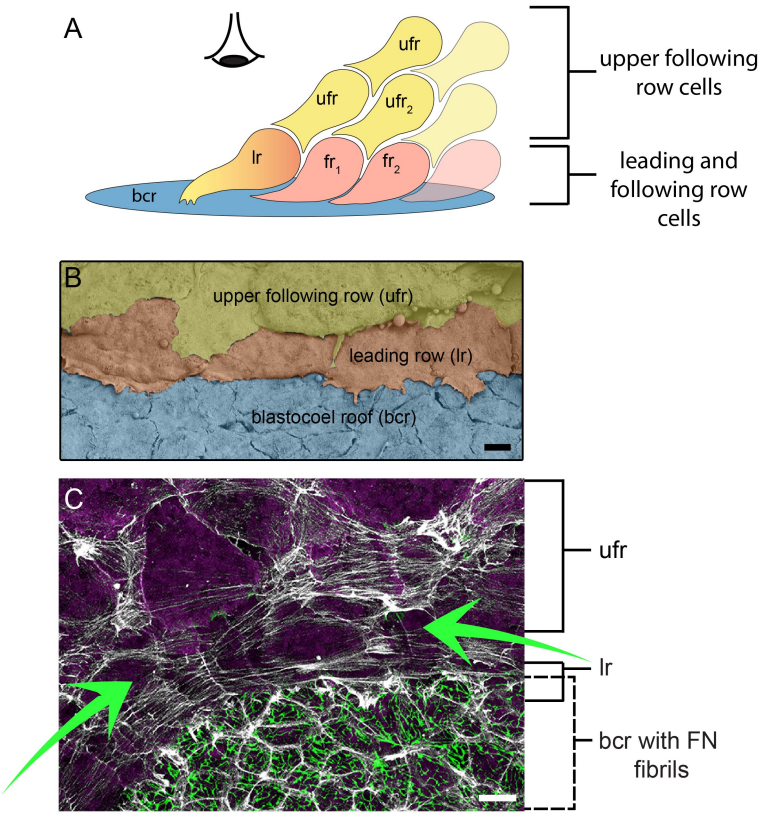

Fig. S7: (A) Cartoon of the organization of mesendoderm cell rows during gastrulation. Perspective of panels B and C are indicated by the eye. The leading row (lr) and following row (fr) cells are in contact with the bcr and fibronectin matrix whereas the upper following rows (ufr) of cells are only in contact with one another. Cells are numbered with respect to their position away from the free edge. (e.g. fr1, ufr2). (B) Scanning electron micrograph of mesendoderm and blastocoel roof tissue excised from a fixed stage 12 embryo. Upper following row cells (yellow) extend protrusions onto the leading row (orange) cells beneath. Scale bar =10µm. (C) Projection of confocal z-sections of stage 12 mesendoderm and blastocoel roof tissue immunostained with antibodies to FN (green) and beta-catenin (magenta). Actin (white) was visualized using phalloidin. Green arrows indicate circumferential forces. ufr, upper following row; lr, leading row; bcr, blastocoel roof. Scale bar=20 µm

Supplementary Movies

Movie 1: Protrusion morphology of leading edge cells: Time lapse TIRF images of leading edge cells expressing mem-EGFP to label cell membrane. Time interval between each frame is 15 secs. Images were collected for 5 mins (Movie is representative of 9 individual explants imaged across 3 separate experiments). Playback rate is 4 frames per second. Scale bar=25um

Movie 2: Specialized filopodia of following row cells: Time lapse TIRF images of following row cells expressing mem-EGFP to label cell membrane. Time interval between each frame is 15 secs. Images were collected for 5 mins (Movie is representative of 9 individual explants imaged across 3 separate experiments). Playback rate is 4 frames per second. Scale bar=25um

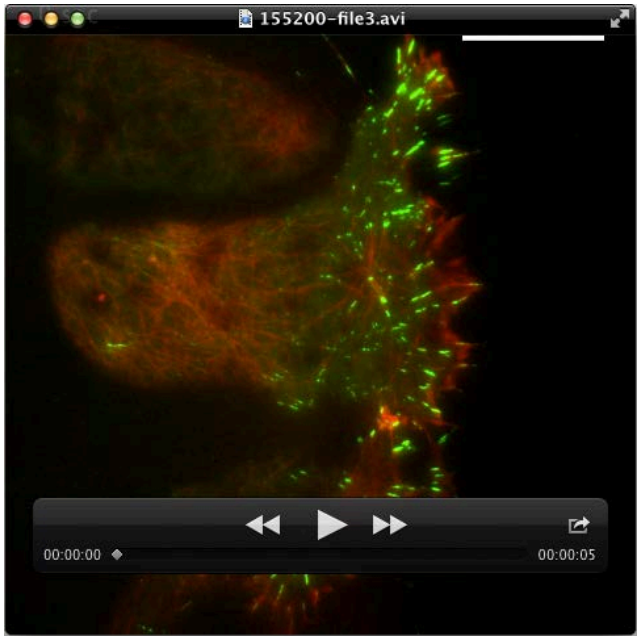

Movie 3: Leading edge mesendoderm cells in controls form stable FAs: Time-lapse TIRF images of control leading edge cells expressing EGFP-paxillin (Green) and LifeAct-mCherry (Red). Time interval between each frame is 15 secs and images were collected for 5 mins (Movie is representative of 9 individual explants imaged across 3 separate experiments). Playback rate is 4 frames per second. Scale bar=25um

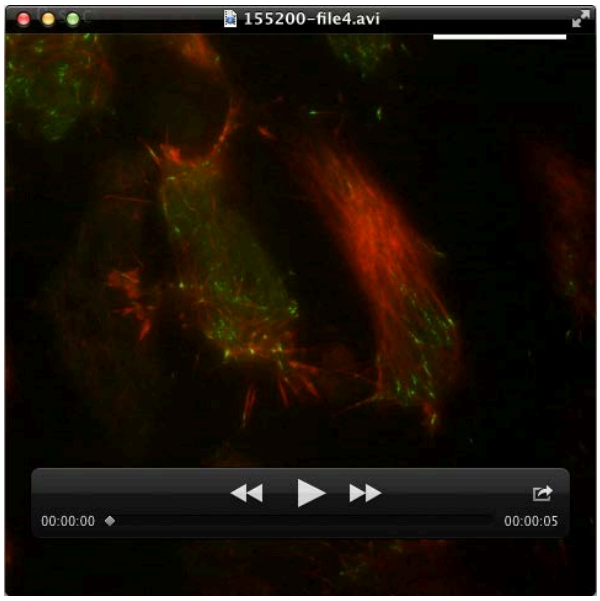

Movie 4: Following row mesendoderm cells in controls form dynamic FAs: Time-lapse TIRF images of control following row cells expressing EGFP-paxillin (Green) and LifeAct-mCherry (Red). Time interval between each frame is 15 secs and images were collected for 5 mins (Movie is representative of 9 individual explants imaged across 3 separate experiments). Playback rate is 4 frames per second. Scale bar=25um

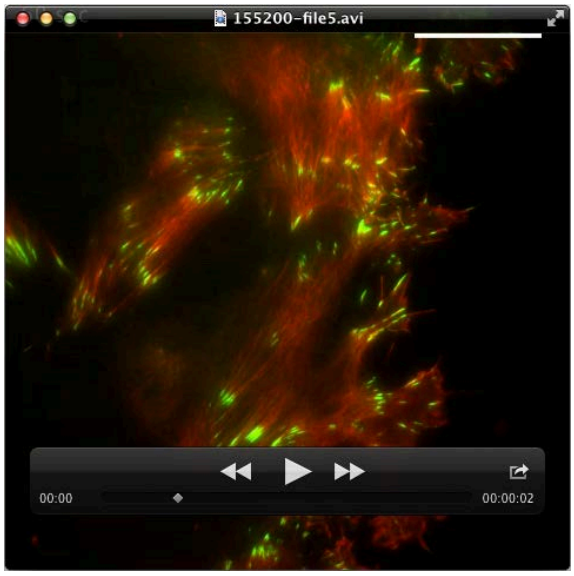

Movie 5: Leading edge cells of krt8 morphant explants form large FAs: Time-lapse TIRF images of krt8 morphant leading edge cells expressing EGFP-paxillin (Green) and LifeAct-mCherry (Red). Time interval between each frame is 30 secs and images were collected for 5 mins (Movie is representative of 9 individual explants imaged across 3 separate experiments). Playback rate is 4 frames per second. Scale bar=25um

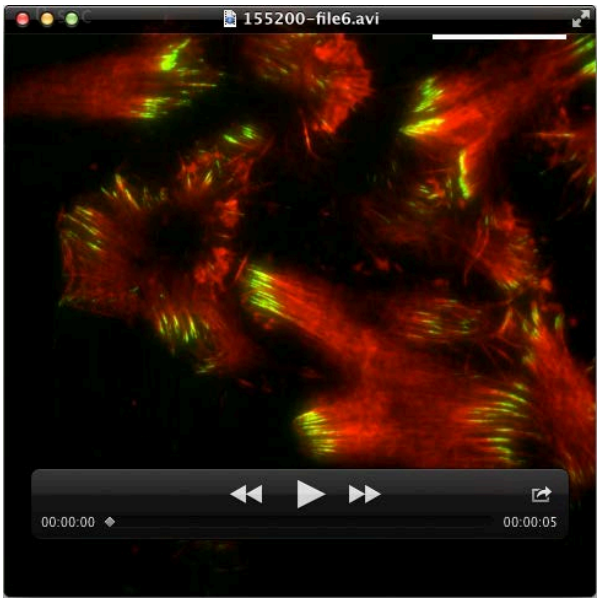

Movie 6: Following row cells of krt8 morphant explants form stable FAs: Time-lapse TIRF images of krt8 morphant following row cells expressing EGFP-paxillin (Green) and LifeAct-mCherry (Red). Time interval between each frame is 30 secs and images were collected for 5 mins (Movie is representative of 9 individual explants imaged across 3 separate experiments). Playback rate is 4 frames per second. Scale bar=25um

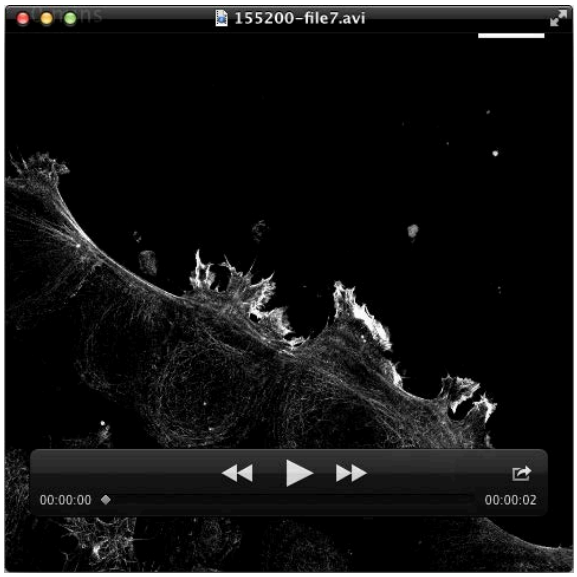

Movie 7: Normal arrangement of actin cytoskeleton associated with migration of control mesendoderm explants: Time-lapse confocal images of a control MO injected mesendoderm explant expressing LifeAct-mCherry. Time interval between each frame is 2 mins and images were collected for 14 mins. Each frame is a collapsed 5um z-stack (Movie is representative of 6 individual explants imaged across 2 separate experiments). Playback rate is 4 frames per second. Scale bar=25um

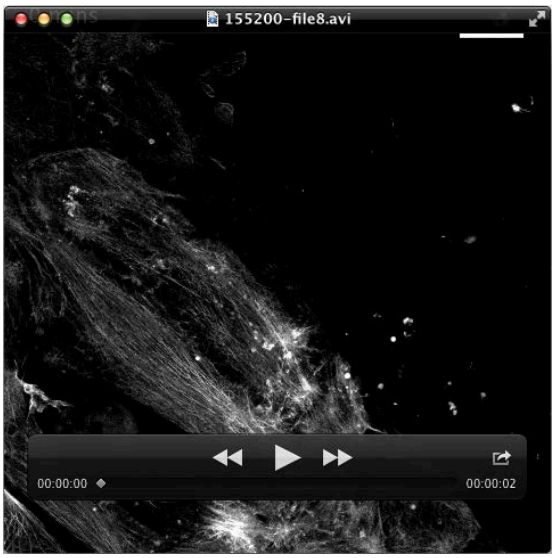

Movie 8: Actin organizes into stress fibers in krt8 morphant explants: Time-lapse confocal images of krt8 morphant mesendoderm explant expressing LifeAct-mCherry. Time interval between each frame is 2 mins and images were collected for 14 mins. Each frame is a collapsed 5um z-stack (Movie is representative of 6 individual explants imaged across 2 separate experiments). Playback rate is 4 frames per second. Scale bar=25um

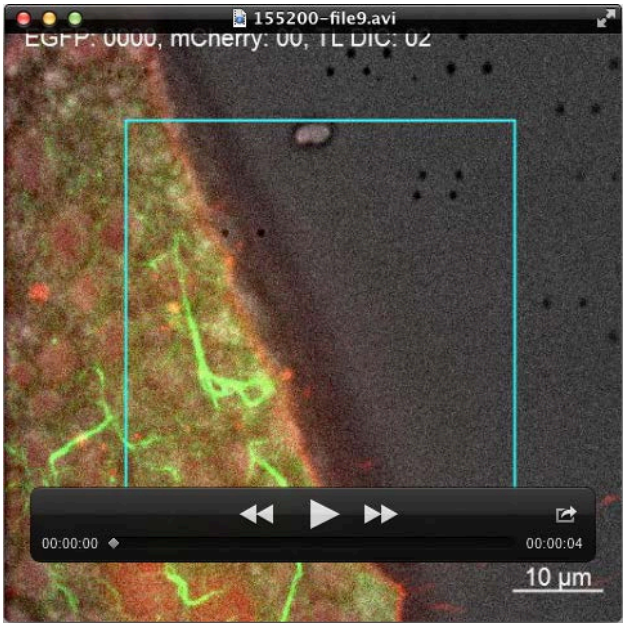

Movie 9: Keratin IFs disassemble upon activation of mCherry-PA-Rac1Q61L: Dissociated mesendoderm cells expressing mCherry-PA-Rac1Q61L (Red) and EGFP-krt8 (Green) were irradiated with a 456nm laser. Box indicates region of activation. Cells were irradiated twice at the same region. Confocal images were taken 15 secs apart. Playback time 4 frames per second (Number of cells analysed = 3). Scale bar=25um

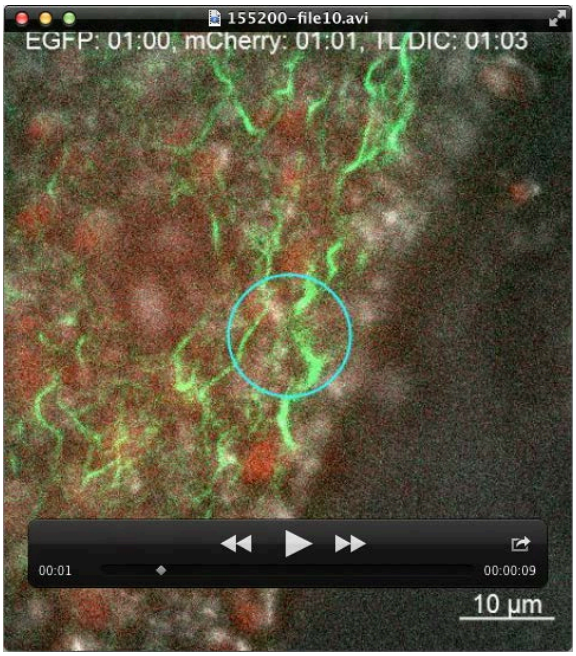

Movie 10: No changes in cell morphologies are observed upon activation of light insensitive mCherry-PA-Rac1C450A: Dissociated mesendoderm cells expressing mCherry-PA-Rac1QC450A (Red) and EGFP-krt8 (Green) were irradiated with 457nm laser. Box indicates region of activation. Images were taken prior to activation. Cells were irradiated twice at the same region. Confocal images were taken 15 secs apart. Playback time 4 frames per second (Number of cells analysed = 3). Scale bar=25um